Food Chemistry: X 37 (2026) 104064

Contents lists available at ScienceDirect

Food Chemistry: X

journal homepage: www.sciencedirect.com/journal/food-chemistry-x

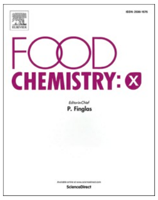

Physicochemical characterisation of iron oxides and hydroxides applied as food additive E 172

Lisa Siciliani [a,b,*], Francesco Fumagalli [c], Jessica Ponti [c], Alessia Bogni [c], Linde Sevenants [a,d], Dario Geebelen [a,e], Noa Olluyn [a,b], Daniela Montalvo [a], Karlien Cheyns [a], Charlotte Wouters [a], Jan Mast [a], Nathalie Claes [b], Sara Bals [b], Eveline Verleysen [a]

[a] *Scientific Department Chemical and Physical Health Risks, Sciensano, Juliette Wytsmanstraat 14, 1050 Ixelles, Belgium*
[b] *Electron Microscopy for Materials Science (EMAT), Universiteit Antwerpen, Campus Groenenborger, Groenenborgerlaan 171, 2020 Antwerp, Belgium*
[c] *European Commission, Joint Research Centre (JRC), Ispra, Italy*
[d] *Department of In Vitro Toxicology and Dermato-Cosmetology, Vrije Universiteit Brussel (VUB), Laarbeeklaan 103, 1090 Jette, Belgium*
[e] *Zoology, Biodiversity and Toxicology, Centre for Environmental Sciences, Universiteit Hasselt, Campus Diepenbeek, Agoralaan, 3590 Diepenbeek, Belgium*

ARTICLE INFO

Keywords:
E 172
Iron oxides
Food additive
Electron microscopy
Physicochemical characterisation
Particle size distribution

ABSTRACT

Within the European Union, iron oxides and hydroxides with specifications defined in Commission Regulation No 231/2012 are allowed as food additive E 172 in numerous food categories. In this work, a detailed physicochemical characterisation of twelve commercially available E 172 iron oxides was performed. Based on material colour, crystal structure and particle shape, four main forms were identified by electron microscopy and X-ray diffraction: red spheroidal hematite; red elongated hematite; yellow elongated goethite; black spheroidal magnetite. Each type contained a fraction of nanoparticles. Raman spectroscopy and X-ray photoelectron spectroscopy identified maghemite at the surface of magnetite particles. Time-of-flight secondary ions mass spectrometry showed differences in surface chemistry and trace contaminants between E 172 forms. Inorganic impurity levels measured by inductively coupled plasma mass spectrometry remained below EU regulatory limits. The results provide insight into the distinct forms that are applied as E 172, and address current data gaps on physicochemical characterisation.

1. Introduction

Iron oxides and iron hydroxides, hereafter termed iron (hydr)oxides, are inorganic substances which can be applied as food additive E 172 in the European Union (EU), with specifications defined in Commission Regulation No 231/2012 (European Commission, 2012). According to Annex II of the Food Additives Regulation (EC) 1333/2008, the use of iron (hydr)oxides as food additive is permitted in numerous food categories at *quantum satis* (European Commission, 2008). Food additive E 172 is applied, amongst others, to colour confectionery, cheese, fish and shellfish paste (European Commission, 2008). In addition, it is used as a contrast enhancer for marking citrus fruits, melons and pomegranates, with a maximum level of 6 mg/L or 6 mg/kg, as appropriate. In the USA, synthetic iron (hydr)oxides are authorised in food for colouring candy, mints, chewing gum and sausages, with a maximum limit of 0.10% of the final weight of the food (CFR—Code of Federal Regulations Title 21. Part 73—Listing of Color Additives Exempt from Certification—Synthetic Iron Oxide (21 CFR 73.200), 2018). Iron oxides can also be applied in food packaging and food contact materials (*BfR Recommendations on Food Contact Materials—BfR, 2025*; CFR—Code of Federal Regulations Title 21. Part 186—Indirect Food Substances Affirmed as Generally Recognized as Safe—Ferric Oxide (21 CFR 186.1300), 2018; CFR—Code of Federal Regulations Title 21. Part 186—Indirect Food Substances Affirmed as Generally Recognized as Safe—Iron Oxides (21 CFR 186.1374), 2018; EFSA Panel on Food Contact Materials, Enzymes, Flavourings and Processing Aids (CEF), 2013; European Commission, 2011).

The EU specifications for E 172 include several iron (hydr)oxide substances related to specific colours:

- yellow iron oxide (hydrated iron (III) oxide), $FeO(OH) \cdot H_2O$, EINECS:257-098-5;

---

* Corresponding author at: Scientific Department Chemical and Physical Health Risks, Sciensano, Juliette Wytsmanstraat 14, 1050 Ixelles, Belgium.
E-mail address: lisa.siciliani@sciensano.be (L. Siciliani).

https://doi.org/10.1016/j.fochx.2026.104064
Received 12 December 2025; Received in revised form 1 June 2026; Accepted 2 June 2026

- red iron oxide (anhydrous iron (III) oxide), Fe_2O_3, EINECS:251-168-2;
- black iron oxide (iron (II, III) oxide), $FeO{\cdot}Fe_2O_3$, EINECS:235-442-5.

Commercially, different hues of E 172 are available as a result of blending yellow, red and black iron (hydr)oxides.

Iron (hydr)oxides were re-evaluated by European Food Safety Authority (EFSA) as food additive in 2015 (EFSA Panel on Food Additives and Nutrient Sources added to Food (ANS), 2015) and as feed additive for all animal species in 2016 (EFSA Panel on Additives and Products or Substances used in Animal Feed (FEEDAP), 2016). Based on their different physical and chemical properties, the Scientific Panel on Food Additives and Nutrient Sources added to Food (ANS Panel) recommended a clear differentiation between the different iron (hydr)oxides, *e.g.*, by adding a, b, c to the E number (EFSA Panel on Food Additives and Nutrient Sources added to Food (ANS), 2015).

Iron (hydr)oxides applied as E 172 are particulate materials and the present EU specifications of E 172 do not limit the particle size, nor the fraction of nanoparticles (European Commission, 2012, 2022). Because of the potential importance of nanoparticles in toxicokinetics and toxicological effects, the ANS Panel considered that the particle size and particle size distribution (PSD) should be included in the specifications of iron (hydr)oxides. Since the publication of the 2015 re-evaluation, only a few studies have investigated the physicochemical properties of iron (hydr)oxides applied as food additive E 172, and their behaviour in biological environments (Favela-Camacho et al., 2019; Sieg et al., 2024; Voss, Hsiao, et al., 2020; Voss, Yilmaz, et al., 2020). Voss et al. analysed seven commercially available E 172 samples of different colours, originating from several countries, using complementary techniques to identify the chemical composition, trace elements impurities, the specific surface area, the zeta potential, and the size distribution of the constituent particles (Voss, Hsiao, et al., 2020). Transmission electron microscopy (TEM) and small-angle X-ray scattering (SAXS) showed that all E 172 samples contained a fraction of small particles including nanoparticles, typically more than 50% (Voss, Hsiao, et al., 2020). Due to magnetic properties, a high degree of agglomeration was observed for black E 172 materials (Favela-Camacho et al., 2019).

In 1980, The Joint FAO/WHO Expert Committee on Food Additives (JECFA) determined an acceptable daily intake (ADI) for iron oxides and hydrated iron oxides of 0–0.5 mg/kg bw/day (JECFA, 1980). Specifications including specific purity criteria for E 172 iron (hydr)oxides were also defined by JECFA in 2008 (JECFA, 2008) and in the EU specifications (European Commission, 2012). In the EFSA re-evaluation of 2015, the ANS Panel recommended a revision of maximum limits for several toxic elements (cadmium, arsenic, lead and mercury) to ensure that iron (hydr)oxides applied as food additive are not a significant source of these toxic elements in food. An additional recommendation was that the limit value for chromium in the EU specifications should be related to chromium (III) only, and that contamination by chromium (VI) should be absent completely.

To address some of the remaining data gaps for the risk assessment of iron hydr(oxides) in line with the EFSA Guidance on Nanomaterials Risk Assessment (EFSA Scientific Committee et al., 2021), this work performed a detailed physicochemical characterisation of a series of commercially available pristine E 172 materials, consisting of the three iron (hydr)oxide substances given in the EU specifications (European Commission, 2012), and their variation in forms, using multiple techniques, including electron microscopy (EM), zeta-potential measurements by electrophoretic light scattering (ELS), X-ray diffraction (XRD), Raman spectroscopy, X-ray photoelectron spectroscopy (XPS), Brunauer, Emmett, and Teller analysis (BET), time-of-flight secondary ions mass spectrometry (ToF-SIMS), inductively coupled plasma mass spectrometry and optical emission spectrometry (ICP-MS/OES). The applied methods aim to differentiate the forms based on their physicochemical properties including particle size and shape distribution, elemental composition, phase, surface properties, volume specific surface area, pore size, and impurities. This work investigates, based on a detailed physicochemical characterisation, whether grouping of E 172 substances is possible in view of specification of the food additive and its risk assessment.

2. Materials and methods

2.1. Materials

Twelve pristine iron (hydr)oxide materials were purchased from multiple suppliers. While some suppliers were located outside of the European Union, the materials were all specifically advertised as red E 172, yellow E 172, black E 172 and brown E 172, and intended for use as food additive E 172 within the EU.

The materials were given an internal reference based on their colour (Table 1). Based on an initial qualitative screening by EM, materials containing multiple forms, hereafter referred to as mixtures, were identified and excluded for further physicochemical characterisation (Table 1). Six materials were selected from detailed characterisation (Table 1), amongst which four were received by the JRC Nanomaterials' Repository (JRC Nanomaterials Repository—European Commission, *n. d.*) for further investigation and possible inclusion in the distribution list, namely with codes: Red1 is E172-JRCNM13104a; Red2 is E172-JRCNM13105a; Yellow2 is E172-JRCNM82106a; Black2 is 172-JRCNM18107a. A table summarising the characterisation methods applied for each specific material is given as supplementary information (Table S.I.1).

2.2. EM analyses

The generic NANOGENOTOX protocol was applied to prepare dispersions of the twelve E 172 materials (Jensen et al., 2011). Briefly, 15.36 mg of iron (hydr)oxide powder was weighed in a 20 mL Wheaton® liquid scintillation vial, pre-wetted with 30 μL of ethanol absolute (VWR International, Leuven, Belgium) and brought in 5.97 mL of an aqueous 0.05% Bovine Serum Albumin (BSA) solution (Sigma-Aldrich, Hoeilaart, Belgium). Probe sonication was applied using a calibrated probe sonicator (Booth & Jensen, 2015) (Vibracell™ 75,041 ultrasonifier, Fisher Bioblock Scientific, Aalst, Belgium) equipped with a 13 mm probe at 20% of amplitude, delivering an energy of 1.17 kJ/mL. To avoid heating, samples were cooled in ice water during sonication. For electron diffraction experiments, a 10 times higher concentration (25.6 mg/mL) was applied, ensuring a larger amount of particles on the EM-grids and a sufficiently high intensity of the powder electron diffraction patterns.

Table 1
Overview of the E 172 samples, including their colour, reference name, shape of their constituent particles (CP) and their crystallographic phase. **Bold**: materials selected for detailed physicochemical characterisation.

Colour	Reference	Descriptive EM: Shape of CP(ECHA, 2022)	Crystallographic phase (XRD and/or electron diffraction)
Red	**Red1**	**Spheroidal (octahedron)**	**Hematite – α-Fe_2O_3**
Red	**Red2**	**Elongated (rod-like)**	**Hematite – α-Fe_2O_3**
Red	**Red3**	**Elongated (rod-like)**	**Hematite – α-Fe_2O_3**
Red	Red4	Spheroidal (octahedron)	Hematite – α-Fe_2O_3
Yellow	**Yellow1**	**Elongated (rod-like)**	**Goethite – α-FeO(OH)**
Yellow	**Yellow2**	**Elongated (rod-like)**	**Goethite – α-FeO(OH)**
Yellow	Yellow3	Elongated (rod-like)	Goethite – α-FeO(OH)
Black	Black1	Mixture	Mixture
Black	**Black2**	**Spheroidal (cube)**	**Magnetite – Fe_3O_4** **Maghemite – γ-Fe_2O_3 at the surface**
Black	Black3	Mixture	Mixture
Brown	Brown1	Mixture	Mixture
Brown	Brown2	Mixture	Mixture

EM specimens (grids) were prepared using the grid-on-drop deposition, by placing Alcian blue pre-treated pioloform- and carbon-coated, 400 mesh copper grids (Agar Scientific, Essex, England) on 20 μL droplets of the dispersions for 10 min (Mast et al., 2015). Afterwards, the grids were blotted dry to remove excess sample and left to air-dry at room temperature. In case no stable dispersion was obtained using the NANOGENOTOX protocol, the drop-on-grid deposition was applied as well (Mast et al., 2015).

EM analyses were performed using a 200 kV Talos F200S G2 transmission electron microscope (TEM) (Thermo Fisher Scientific, Eindhoven, The Netherlands), equipped with a Ceta 16M camera, high angle annular dark field (HAADF) and Super-X detectors using Velox software (Version 3.12, Thermo Fisher Scientific, Eindhoven, The Netherlands).

Qualitative high angle annular dark field – scanning transmission electron microscopy (HAADF-STEM) analysis was performed to evaluate the applied sample preparation, to determine the particle properties and to evaluate whether one or multiple forms of iron (hydr)oxide particles are present. For each E 172 material, a set of calibrated selected and representative HAADF-STEM micrographs showing the size and shape of the constituent particles and their agglomeration state were recorded. A scan size of 1024 × 1024 pixels, a dwell time of 20 μs, a probe convergence angle of 10.5 mrad, and a camera length of 260 mm were applied. Particle shapes were described qualitatively following ECHA Guidance (ECHA, 2022).

Energy dispersive X-ray spectroscopy (EDX) analysis was applied to determine the elemental composition of the particles and to verify if other types of inorganic particles were present. Spectra and spectral images were recorded under the same conditions as applied for HAADF-STEM imaging for 126 s with 5 frames.

To determine the crystal structure of the observed particles, selected area electron diffraction (SAED) patterns of regions containing a large number of particles were recorded and indexed using databases (Jain et al., 2013; Yibin et al., 2011). A diffraction pattern of colloidal gold nanoparticles was measured to calibrate the camera length.

Quantitative measurement of particle size and shape distributions was performed in HAADF-STEM mode using a scan size of 2048 × 2048 pixels, a dwell time of 10 μs, a probe convergence angle of 10.5 mrad, and a camera length of 260 mm. For each material, a magnification suitable for the quantitative analysis was determined following CEN TS 17273 (Nanotechnologies - Guidance on Detection and Identification of Nano-Objects in Complex Matrices, 2018) and ISO 13322-1 (Particle Size Analysis — Image Analysis Methods — Part 1: Static Image Analysis Methods, 2014, p. 1), such that the minimum Feret diameter of most of the analysed particles was larger than the lower limit of quantification (LLOQ), which is defined as ten times the pixel size, and smaller than the upper limit of quantification (ULOQ), which is defined as one tenth of the image size (Table S.III.1 in supplementary information). At least 30 images were acquired randomly and systematically over the entire grid area, and a stage shift was applied centring the particles of interest. At least 300 particles were measured per sample, in accordance with Wouters et al. (2025).

The size and shape properties of the constituent particles were measured manually based on the properties of their 2D projections using ImageJ software (Schindelin et al., 2012). The polygon selection tool was used to measure the minimum and maximum Feret diameters and aspect ratio (AR) simultaneously using counting rule 4 (Bresch et al., 2022) as illustrated in the supplementary information (Figs. S.IV.1 and S.IV.2). The raw data resulting from the image analysis was processed using an in-house MATLAB (version 24.2.0 (R2024b), The MathWorks Inc., Natick, Massachusetts, USA) script for calculation of descriptive statistics and plotting histograms. For all samples, the number-based distributions and the kernel density estimates (KDE) were determined using MATLAB. Bin width was calculated using the Freedman-Diaconis rule (Freedman & Diaconis, 1981). For the KDE plot, producing a continuous density estimate, a Gaussian kernel was applied. For each dataset, the mean, modal and median values and D10, D25, D75 and D90 percentiles were calculated (Table 2). In addition, the percentage of particles smaller than 100 nm, the percentage of particles smaller than 250 nm of the fraction below 500 nm, and the percentage of particles with an AR larger than 3 were determined.

Measurement uncertainties were determined based on a validation study on materials Red1 and Yellow2, selected as representative materials for spheroidal and elongated E 172 iron (hydr)oxides, respectively. Expanded measurement uncertainties were determined as described by Verleysen et al. (Verleysen et al., 2019), and include uncertainties associated to repeatability, day-to-day variation, calibration and trueness. The expanded measurement uncertainty does, however, not include possible systematic bias originating from, *e.g.*, sampling or image analysis.

For materials containing pores within their particles, electron tomography was performed in HAADF-STEM mode using a Tecnai G2 electron microscope operated at 200 kV. The tilt series were acquired over an angular range of ±70°, with a tilt increment of 3°. The reconstructions were performed with the ASTRA toolbox, available for MATLAB (van Aarle et al., 2015; van Aarle et al., 2016). Six tomograms were analysed: three for Red2 and three for Red3. The pore sizes were measured on the ".rec" file, resulting from the reconstruction, using ImageJ software (Schindelin et al., 2012). To determine the pore size, a first mask of the reconstruction consisting of the full volume of the particles, including the pores, was generated. A second mask containing only the volume of the particles, excluding the pores, was created. Both masks were then subtracted into a new file showing only the pore volume (see Fig. S.V.1 in supplementary information). The pores were measured automatically using the Analyse Particles tool in ImageJ. The raw data resulting from the analysis was processed using an in-house MATLAB (version 24.2.0 (R2024b), The MathWorks Inc.) script to determine the size of the pores.

2.3. *Zeta potential measurements by ELS*

25.6 mg iron (hydr)oxide powder was brought in 10 mL MilliQ water (Arium® pro DI/UV equipment, Sartorius, Göttingen, Germany) and sonicated using a calibrated probe sonicator (Booth & Jensen, 2015) (Vibracell^{TM} 75,041 ultrasonifier, Fisher Bioblock Scientific) equipped with a 13 mm probe at 20% of amplitude, delivering an energy of 0.7 kJ/mL. Samples were cooled in ice water during sonication. The dispersions were further diluted by bringing 4 mL in 36 mL MilliQ water. ELS (Zetasizer Nano ZS, Malvern Panalytical, Malvern, UK) was performed in triplicate to monitor the zeta potential in aqueous medium as a function of pH. The measurements were performed from pH 7 to pH 2 by decreasing the pH using HCl, and from pH 7 to 12 by increasing the pH using NaOH. The pH was monitored using a pH meter (SevenCompact, Mettler Toledo, Zaventem, Belgium).

2.4. *XRD*

To determine their crystal structure by XRD, iron (hydr)oxide powders were pressed onto a powder analysis sample holder using glass tools and analysed without further preliminary treatments. XRD patterns were recorded using a D8 Advance diffractometer (Bruker Gmbh, Germany), operated in a parallel beam configuration (X-ray source settings, $I = 40$ mA and V = 40 kV, wavelength Cu Kα 1.54 Å). A Göbel mirror, a 2.5° Soller collimator, and a 0.6 mm slit were inserted along the primary beam path. A 0.6 mm slit and a 2.5° Soller collimator were mounted on the secondary beam path. 2θ ranged from 6 to 80°, the step size was 0.02°, and the time per step was 5 s. Acquisition scan was performed in 2θ/θ, symmetric (coupled) mode. All raw datasets were treated subtracting amorphous background bands from substrate and air scattering contributions. Crystallite size was determined using Scherrer method (Artusio et al., 2021; Braniste et al., 2020). Each material was measured in three replicates.

Table 2
Summary of the descriptive statistics of the PSD of indicated materials. Black2 (1) and Black2 (2) correspond to the samples of material Black2 obtained by grid-on-drop and drop-on-grid depositions, respectively.

Reference	Red1	Red2	Red3	Yellow1	Yellow2	Black2 (1)	Black2 (2)
	Minimum Feret diameter[a]						
N	311	303	321	300	317	307	333
D10 (nm)	50 ± 14	52 ± 22	57 ± 24	41 ± 17	23 ± 10	79 ± 23	94 ± 27
D25 (nm)	65 ± 13	65 ± 24	76 ± 28	64 ± 23	40 ± 15	107 ± 22	121 ± 24
D50 (median) (nm)	88 ± 11	88 ± 16	106 ± 19	96 ± 17	72 ± 13	139 ± 18	170 ± 22
D75 (nm)	123 ± 18	131 ± 17	154 ± 20	154 ± 19	106 ± 13	191 ± 29	213 ± 32
D90 (nm)	155 ± 23	205 ± 36	231 ± 41	206 ± 36	156 ± 28	245 ± 36	271 ± 40
Mean (nm)	97 ± 12	113 ± 15	131 ± 17	111 ± 15	82 ± 11	157 ± 19	178 ± 21
Mode (nm)	77 ± 26	69 ± 23	83 ± 27	73 ± 24	67 ± 22	122 ± 41	172 ± 58
Fraction<100 nm (%)	60	60	45	51	72	20	13
Fraction<250 nm (%)	100	94	91	98	99	91	86
Fraction<LLOQ (%)	0	0	0	0	3	0	0
Fraction>ULOQ (%)	0	4	4	0	0	3	3
	Maximum Feret diameter[a]						
N	311	303	321	300	317	307	333
D10 (nm)	98 ± 26	150 ± 81	146 ± 80	155 ± 85	125 ± 68	110 ± 29	127 ± 34
D25 (nm)	129 ± 21	225 ± 77	284 ± 97	224 ± 77	247 ± 84	144 ± 23	164 ± 26
D50 (median) (nm)	166 ± 15	344 ± 70	459 ± 93	313 ± 63	372 ± 75	192 ± 17	225 ± 20
D75 (nm)	206 ± 14	520 ± 133	629 ± 161	449 ± 115	535 ± 137	258 ± 18	299 ± 21
D90 (nm)	228 ± 18	734 ± 183	850 ± 212	611 ± 152	844 ± 210	338 ± 26	375 ± 29
Mean (nm)	165 ± 15	403 ± 92	480 ± 109	354 ± 81	433 ± 99	213 ± 20	244 ± 23
Mode (nm)	159 ± 48	292 ± 61	495 ± 103	275 ± 57	368 ± 77	156 ± 47	212 ± 64
Fraction<LLOQ (%)	0	0	0	0	0	0	0
Fraction>ULOQ (%)	10	55	68	75	61	12	21
	Aspect ratio[a]						
N	311	303	321	300	317	307	333
D10	1 ± 0.1	2 ± 0.3	2 ± 0.3	2 ± 0.2	3 ± 0.4	1 ± 0.1	1 ± 0.1
D25	1 ± 0.2	3 ± 0.4	3 ± 0.4	2 ± 0.3	4 ± 0.5	1 ± 0.2	1 ± 0.2
D50 (median)	2 ± 0.1	4 ± 0.5	4 ± 0.5	3 ± 0.5	5 ± 0.7	1 ± 0.1	1 ± 0.1
D75	2 ± 0.2	5 ± 0.7	5 ± 0.7	5 ± 0.8	7 ± 1.0	1 ± 0.1	1 ± 0.1
D90	2 ± 0.2	6 ± 0.9	7 ± 1.0	7 ± 1.1	10 ± 1.5	2 ± 0.1	2 ± 0.1
Mean	2 ± 0.1	4 ± 0.6	4 ± 0.6	4 ± 0.6	6 ± 0.9	1 ± 0.1	1 ± 0.1
Mode	2 ± 0.5	3 ± 0.5	3 ± 0.5	2 ± 0.3	4 ± 1.5	1 ± 0.4	1 ± 0.4
Fraction AR > 3 (%)	1	65	65	53	88	1	0

[a] Measurement uncertainties are expanded uncertainties (k = 2) with a confidence level of 95%.

2.5. Raman spectroscopy

Iron (hydr)oxide powders were pressed on soda-lime glass slides and analysed with the inViaTM Confocal Raman microscope (Renishaw, New Mills, UK). Acquisition parameters for Raman spectra were optimised as follows: focusing optics magnification: 50×, laser wavelength: 530 nm (green), gratings: 1800 ln/mm, accumulation time: 1 s, laser power: 10%, number of spectral accumulations: 10. Spectra were recorded in the 100–3000 cm^{-1} spectral range. The powder spectra were assigned after baseline subtraction of the acquired raw spectra using WiRE 5.5 software (Windows-based Raman environment, Renishaw) by comparison with reference database spectra (Valsesia et al., 2021).

2.6. XPS

Surface chemical composition was investigated by XPS (AXIS ULTRA, DLD Kratos Analytical, Manchester, UK) equipped with a monochromatic Al Kα source ($h\nu = 1486.6$ eV) operating at 15 mA, 15 kV. Samples for XPS analysis were applied onto O_2 plasma cleaned silicon substrate wafers equipped with a 5 × 5 mm copper adhesive substrate. Sample preparation and analysis methods followed the recommendations for the “stick and go” method from Bennet et al. (Bennet et al., 2020, 2023). Wide scan spectra were recorded from 1250 to 0 eV binding energy in hybrid mode, full slit aperture (400 × 700 μm^2 analysis area), and at 80 eV pass energy, whereas core level spectra were recorded using a pass energy of 20 eV. The take-off angle (ToA), respectively to the sample normal, was 0° for survey and high-resolution (HR) spectra. The operating pressure was 6×10^{-7} Pa. Surface charging was compensated using low energy (~5 eV) electrons and adjusted using the charge balance plate on the instrument. Three different spots were analysed for each sample. All the spectra were processed with CasaXPS (Version 2.3.25) (Fairley et al., 2021). Spectra were calibrated setting hydrocarbon C1s at 285.0 eV. The surface composition was evaluated from the survey spectra, after a Shirley-type background subtraction using the relative sensitivity factors provided by the manufacturer. Peak fitting was performed with no preliminary smoothing. Symmetric Gaussian–Lorentzian (70% Gaussian and 30% Lorentzian) product functions were used to approximate the line shapes of the fitting components (Braniste et al., 2020; Winkler et al., 2022).

The oxidation states of the surfaces of the iron (hydr)oxide particles were determined and quantified, in particular by high resolution measurements of the Fe 2p core-level region exhibiting two main peaks, Fe 2p3/2 and Fe 2p1/2, splitting due to spin-orbit coupling. Deconvolution of the Fe 2p 3/2 peak shape exhibiting multiplet splitting was performed according to the reference methods and values reported in Biesenger et al. (Biesinger et al., 2011) and citations therein.

2.7. BET

The specific surface area (SSA) was measured by nitrogen (N_2) sorption using a GEMINI VII instrument (Micrometrics, Alfatest SRL, Milan, Italy). Before the analysis, each powder was weighted in the amount between 100 and 300 mg in specific glass tubes, and dehydrated, under vacuum, at 60 °C overnight and at 200 °C for 2 h. Three independent runs were considered. Measurements and results were acquired and elaborated by GEMINI VII software (version 3.04, Alfatest

SRL, Milan, Italy). Results were expressed as BET specific surface area (m^2/g) and as VSSA (Volume Specific Surface Area) (g/cm^3) using density corresponding to each material (Table 3).

Table 3
Summary of the SSA and VSSA results assessed by BET.

Sample	SSA ± SD (m^2/g)	VSSA BET (m^2/cm^3)	Density (g/m^3)
Red1	10.8 ± 1.3	56.8 ± 6.9	5.24
Red2	9.9 ± 0.6	52.0 ± 3.4	5.24
Red3	9.3 ± 0.1	49.3 ± 0.4	5.24
Yellow2	20.3 ± 1.1	86.2 ± 4.6	4.25
Black2	5.9 ± 0.1	30.6 ± 0.7	5.17

2.8. ToF-SIMS

ToF-SIMS was performed for the analysis of macromolecular chemistry. Multivariate analysis (MVA) of ToF-SIMS mass spectra was applied to highlight subtle chemical differences within the samples' chemical composition. Samples were prepared as for XPS analysis described previously, and measured with a TOF-IV spectrometer (IONTOF, Münster, Germany). At least 7 mass spectra (for both positive and negative polarity) were acquired on each sample using a 25-keV Bi_3^+ primary ion beam operated in high-current bunched mode. The sample surface was pre-cleaned for 60 s using a GCIB Argon cluster ions source (Ar1300+, 2 keV) to eliminate surface contaminations before the measurements (Bañuls-Ciscar et al., 2020). For analysis, following settings were applied: a field of view of 128 × 128 pixels, random raster, interlaced, 87 scans, dose density 5×10^{11} cm^{-2}, 100 μs cycle time, for both positive and negative secondary ions polarities. Due to the insulating properties of the specimens, a low-energy electron flood gun was used to eliminate charge build up on the surface during analysis. The raster area was 300 × 300 μm^2 for analysis and 800 × 800 μm^2 for Ar-cluster sputtering avoiding any potential edge effect. Spectra were calibrated using [C^+], [CH^+], [CH_2^+], [CH_3^+], [$C_3H_3^+$] and [$C_7H_7^+$] peaks for positive polarity and [CH^-], [C_2H^-], [C_4H^-], [$C_3H_3O_2^-$] for negative polarity. Data post treatment and analysis as well as principal component analysis (PCA) were performed on all dataset using built-in routines in Surface Lab 7.2 (ION-TOF). The PCA approach was based on the selection and identification of about 200 individual mass peaks in the 1–1000 uma range, with the following settings: XY binning none, Z binning sum all scans, spatial scaling none, spectral scaling root mean, centring spectral mean, four considered factors (Bañuls-Ciscar et al., 2020; Bennet et al., 2023).

2.9. ICP-MS/OES

ICP-MS/OES was performed to determine the total concentration of selected inorganic impurities present in the materials, as well as the total mass fraction of iron (Fe). Approximately 150 mg of the samples were digested using 4 mL nitric acid (67–69% HNO_3 Pico-Pure, Chemlab, Belgium) and 4 mL of MilliQ water in a microwave (MARS 6, CEM Corporation, Matthews, NC, United states) at 1600 V. The samples were heated in two stages: at 180 °C for 20 min, and at 200 °C for 20 min. After mineralisation, the digested solution was transferred into 50 mL polypropylene tubes (Sarstedt, Nümbrecht, Germany) and further diluted with MilliQ water. Quantification of Aluminium (Al) and Fe was done by ICP-OES (Varian 720, Santa Clara, CA, United States). Quantification of arsenic (As), cadmium (Cd), chromium (Cr), nickel (Ni), lead (Pb), copper (Cu) and zinc (Zn) was done by triple quadrupole ICP-MS (Agilent 8800, Santa Clara, CA, United States). Arsenic was analysed on mass shift mode (m/z 75–91) using oxygen (O_2) in the reaction cell, Cd (m/z 114–114), Cr (m/z 52–52), Cu (m/z 63–63), Ni (m/z 60–60), Pb (m/z 206–206) and Zn (m/z 66–66) were measured on mass in the helium (He) collision mode. Procedure blanks and in-house quality controls were included for both ICP-OES and MS measurements. The combined uncertainty is estimated based on the trueness and the precision, which were determined by analysing samples that were spiked at two different levels on three separate days. The LOQ was determined based on the standard deviation of the measured concentrations after analysis of 20 procedure blanks.

3. Results

3.1. Material screening by descriptive EM

The NANOGENOTOX dispersion protocol allowed dispersing all yellow and red E 172 materials. Based on visual inspection, the dispersions remained stable for at least 1 h. The NANOGENOTOX protocol did not result in stable dispersions for Black2, and precipitation was observed immediately after sonication. For the brown E 172 materials, expected to be mixtures, partial dispersion/precipitation was observed, as well as for Black1 and Black3 materials.

Drop deposition of red and yellow E 172 materials resulted in even distributions of particles on positively charged EM copper grids, and both isolated particles and small agglomerates were observed (Fig. S.II.1 in supplementary information). Amongst the red E 172 materials, two distinct particle shapes were observed: particles of Red1 and Red4 materials had a spheroidal (octahedron) shape (Fig. 1A and D), while particles of Red2 and Red3 materials had an elongated (rod-like) shape (Fig. 1B and C) (ECHA, 2022). The elongated (rod-like) particles observed in Red2 and Red3 contained pores, visible on the HAADF-STEM images as darker spots. Yellow E 172 samples contained particles with an elongated (rod-like) shape (ECHA, 2022), and showed only minor morphological differences between materials (Fig. 1E–G). Materials Red4 and Yellow3 were excluded from extended physicochemical characterisation, because of their similarity in particle size and shape with materials Red1 and Yellow2 samples, respectively, and their limited available quantity.

Even though dispersions of black and brown E 172 materials were (partly) unstable, particles were present on the TEM grids. It was observed that material Black2 contains only one type of particles (Fig. 1H) while materials Brown1, Brown2, Black1 and Black3 are mixtures (Fig. 1I–L). The constituent particles observed in Black2 have a spheroidal (cubic) shape and are strongly agglomerated (Fig. S.II.2 in supplementary information). Based on the colour of the dispersions and the morphologies of the particles present on the TEM grids, brown materials were considered mixtures of red, yellow, and black iron (hydr) oxides (Fig. 1K and L), while Black1 and Black3 materials were mixtures of yellow and black iron oxides (Fig. 1I and J). All mixtures were excluded from further in-depth physicochemical characterisation (Table 1).

EDX analysis confirmed that the observed particles in all screened E 172 materials contain iron (as illustrated for material Red1 in Fig. S. VII.2 in supplementary information).

3.2. Zeta potential curves

The zeta potential curves of the E 172 materials are similar, apart from material Red3 for which the zeta potential curve is more negative in the acidic pH range (Fig. 2). All other E 172 materials exhibit a zeta potential between −30 mV and +30 mV at neutral pH (Fig. 2), indicating poor dispersion stability in water, and the need for additional stabilisation when preparing dispersions using, *e.g.*, the NANOGENOTOX protocol.

3.3. Crystallographic structure by XRD, electron diffraction, Raman spectroscopy and XPS analyses

The electron diffraction and XRD results are consistent for all six selected materials (Fig. 3). The electron diffraction and XRD data of red, yellow and black E 172 materials match with hematite (α-Fe_2O_3, iron

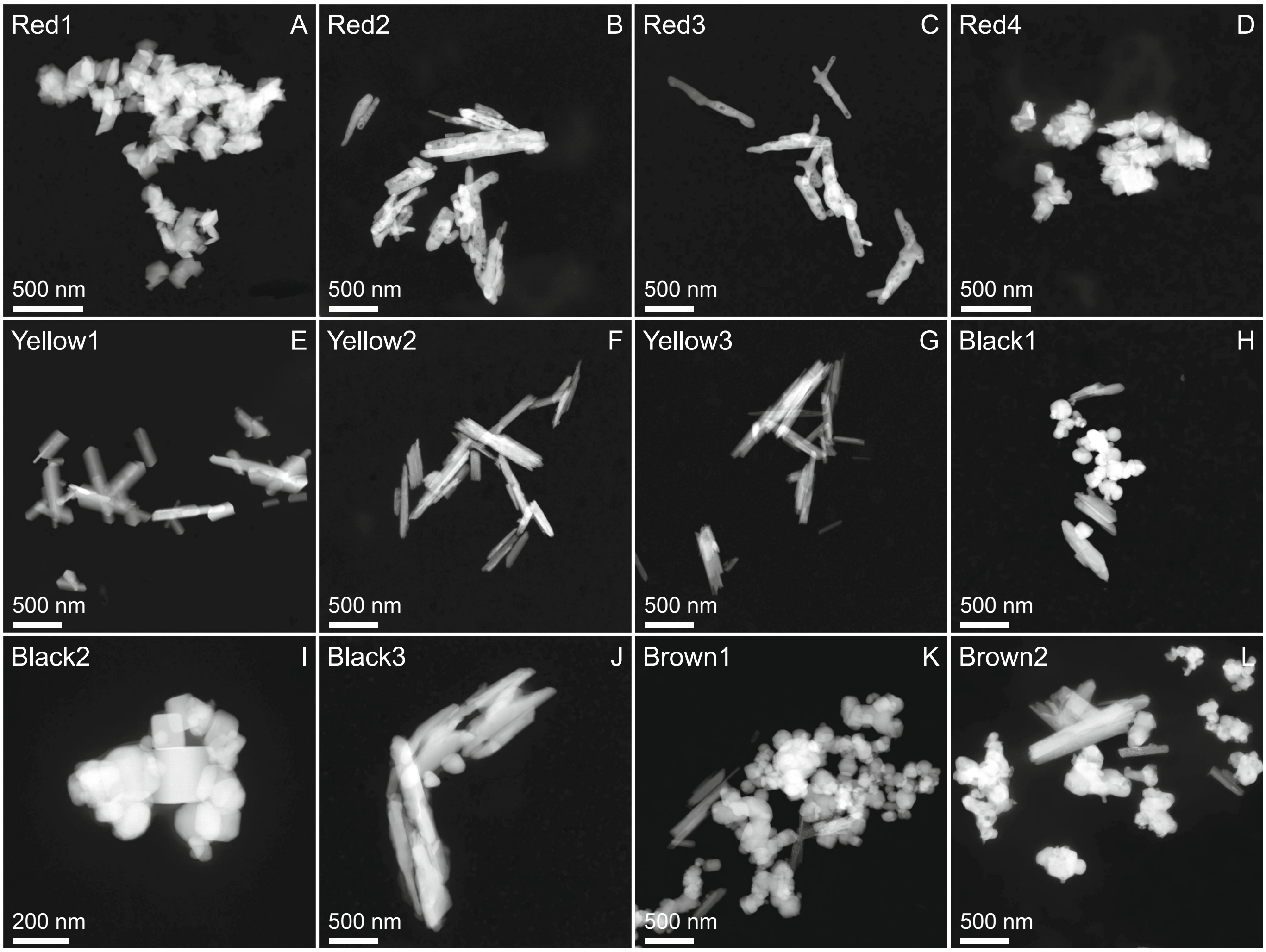

Fig. 1. Representative HAADF-STEM images of the particles observed in the E 172 materials dispersed using the NANOGENOTOX protocol.

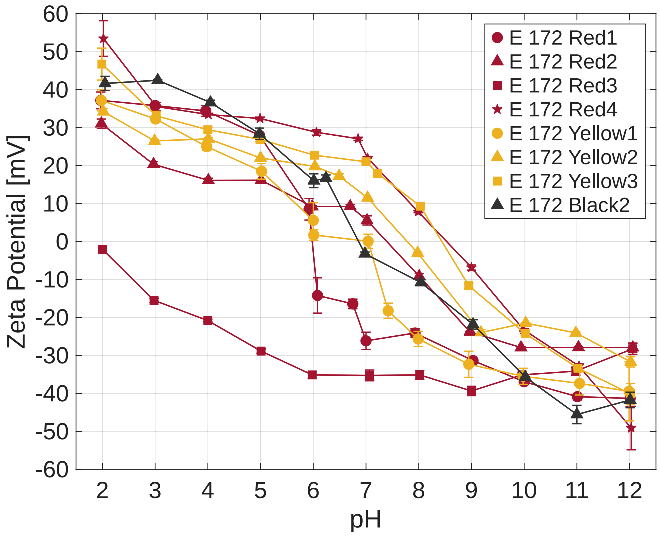

Fig. 2. Zeta potential curves of the E 172 materials in MilliQ water, excluding mixtures. Error bars correspond to the standard error of mean based on triplicate measurements.

(III) oxide), goethite (α-FeO(OH)) and magnetite (Fe_3O_4, iron(II,III) oxide), respectively (Table 1). XRD analysis showed that the crystallinity was higher than 99% for all samples indicating that phases are pure in all cases, with crystallite size in the range of 3–10 nm.

Fig. 4A illustrates XPS high-resolution data of the Fe 2p core-level region for selected E 172 materials of each colour (Red1, Yellow1 and Black2). Evaluation of synthetic fitting peaks allowed to calculate the contribution of each oxidation state to the exposed nanoparticle surface (Fig. 4B). XPS showed mainly hematite and goethite to be present at the surface of the examined red and yellow E 172 materials, respectively, in line with the electron diffraction and XRD results. A small percentage (<10%) of FeO was observed at the surface of red E 172 materials by XPS, while Raman spectroscopy observed a superimposition of other spectral features for Yellow1 (Fig. S.III.1 in supplementary information). XPS semi-quantitative analysis of Black2 surface (depth of analysis of 6.5 ± 1 nm) yielded an at.% composition of mainly maghemite (γ-Fe_2O_3) (72 ± 14%) and partially magnetite (Fe_3O_4) (28 ± 5%) (Fig. 4 B). The presence of a maghemite phase overlayer in Black2 was qualitatively confirmed by the presence of maghemite characteristic vibrational bands in the Raman spectrum of Black2 (depth of field <2 μm), suggesting a mixture of magnetite and maghemite.

3.4. Particle size and shape distributions

The magnification was optimised so that the vast majority of the minimum Feret diameter measurements of the constituent particles of the different E 172 materials lies between the LLOQ and the ULOQ: the

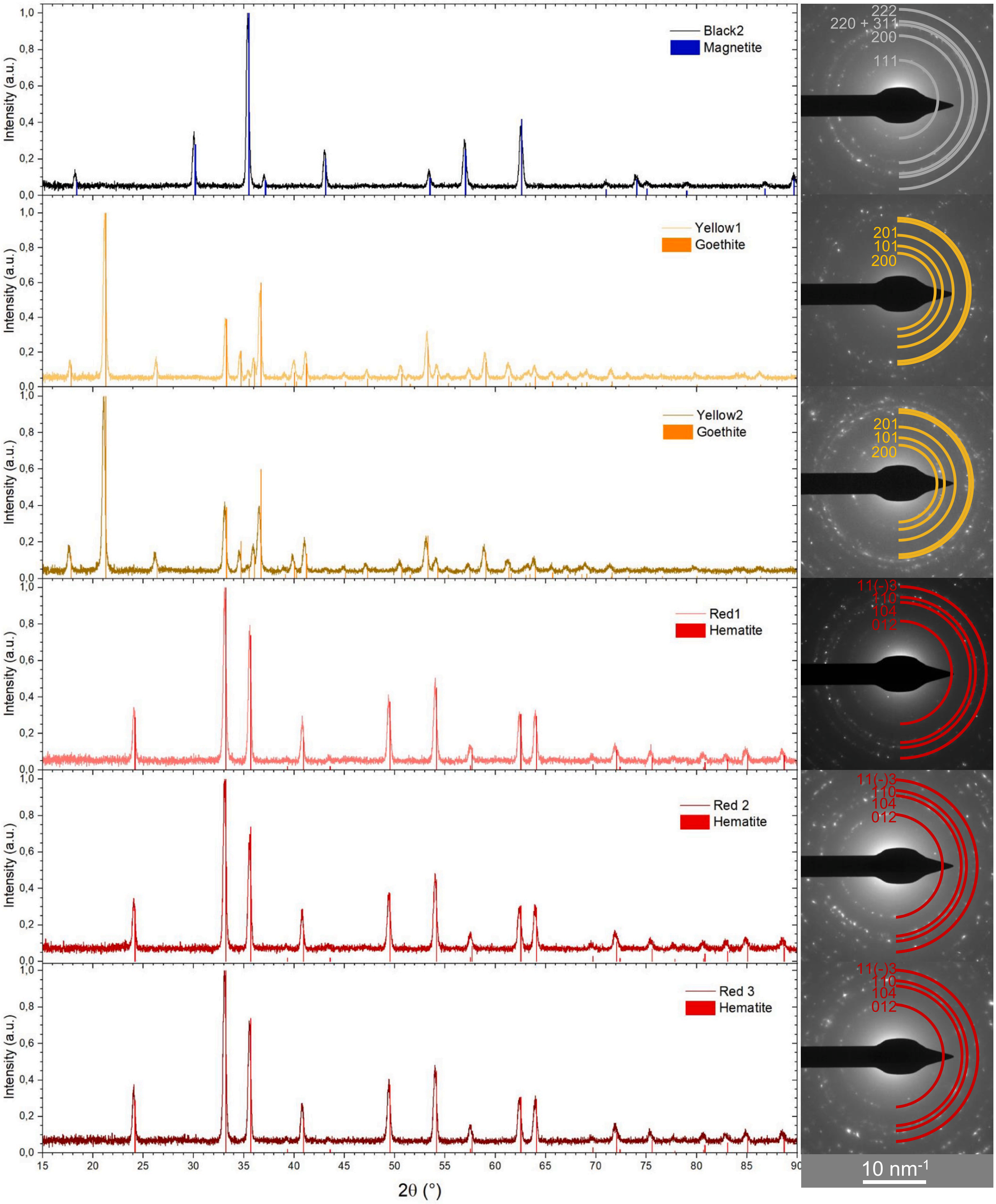

Fig. 3. XRD patterns and SAED patterns of the E 172 materials.

fraction of particles with a minimum Feret diameter below the LLOQ ranges from 0% to 3%, and the fraction above the ULOQ ranges from 0% to 4% (Table 2). For the E 172 materials with spheroidal particles (Black2 and Red1; AR $<$ 3), 10%–21% of particles had a maximum Feret diameter above the ULOQ. For the E 172 materials consisting of elongated particles (Yellow1, Yellow2, Red2 and Red3; AR $>$ 3), 55%–75% of particles had a maximum Feret diameter above the ULOQ. By applying a stage shift to centre the particles of interest on the images, the

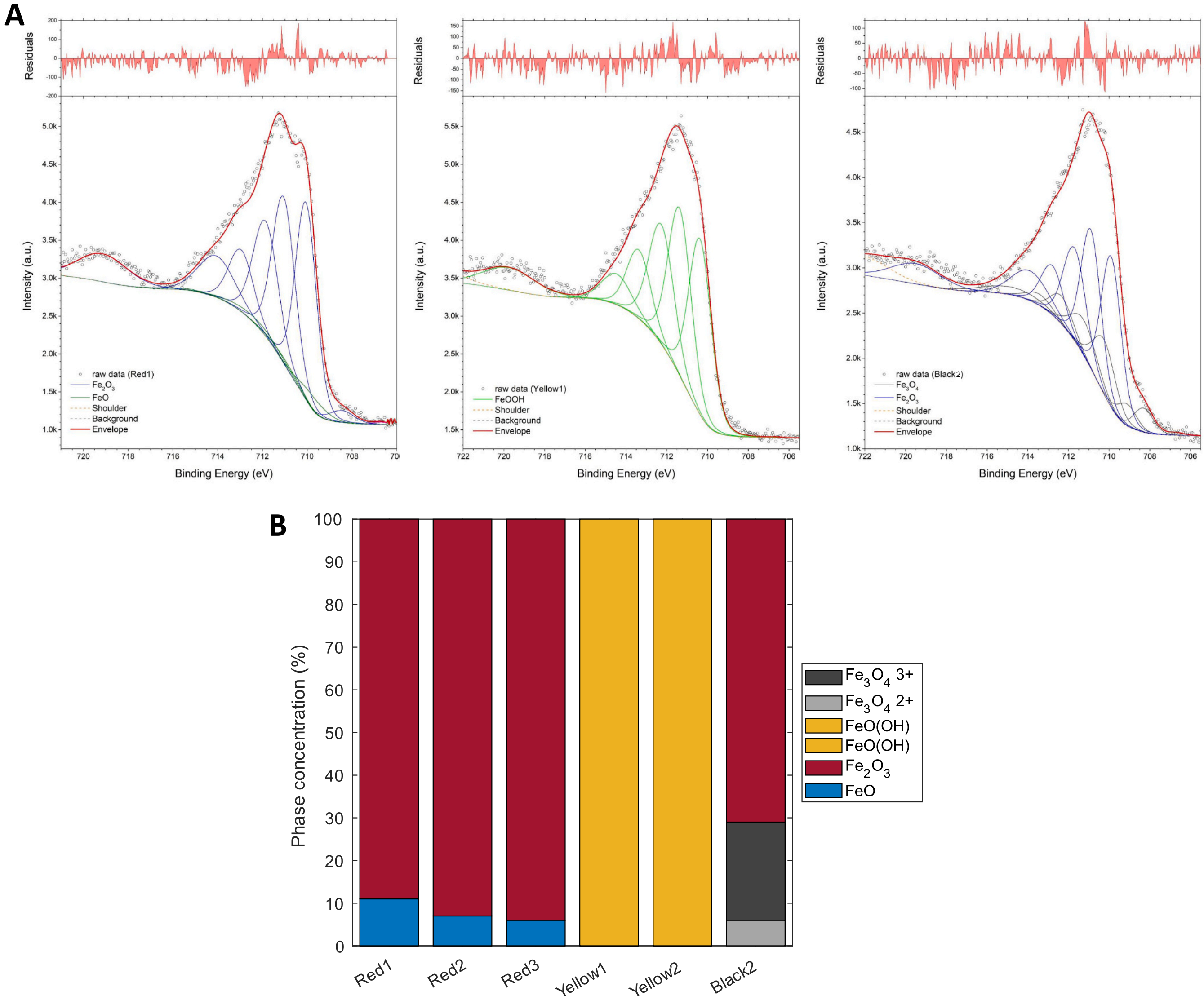

Fig. 4. (A) Illustration of high resolution spectral data for Red1, Yellow1 and Black2, in the binding energy (BE) range 705–722 eV (black circles), which covers the Fe 2p 3/2 peak structure and satellite features and the synthetic model envelope (full red line) and the corresponding multiplets individual peaks for each oxidation state (full coloured lines). In the top part of each panel the absolute intensity of the model residuals is plotted against BE. (B) Evaluation of synthetic fitting peaks allowed to calculate the contribution of each oxidation state to the exposed nanoparticle surface. (For interpretation of the references to colour in this figure legend, the reader is referred to the web version of this article.)

particles were always completely within the field of view, and the maximum Feret diameter was always below the ULOD.

The distributions of the minimum Feret diameter, maximum Feret diameter and aspect ratio resulting from the quantitative HAADF-STEM analysis of the selected E 172 materials are given as supplementary information (Figs. S.IV.3–5). The corresponding descriptive statistics are presented in Table 2.

The quantitative HAADF-STEM analyses shows that all the characterised materials contain a fraction of particles with a minimum Feret diameter smaller than 100 nm, with percentages ranging from 13% (Black2) to 72% (Yellow2). Of the fraction of particles smaller than 500 nm, the percentage of particles with a minimum Feret diameter smaller than 250 nm ranges from 86% to 100%. Elongated E 172 materials (Yellow1, Yellow2, Red2 and Red3) are characterised by a median AR between 3 and 5, whereas the spheroidal materials (Black2 and Red1) resulted in a median AR between 1 and 2. The percentage of particles with an AR larger than 3 ranges from 53% to 88% for elongated materials and is 1% for spheroidal materials.

For Black2, the instability of the dispersion and the low amount of particles on the grids limit the confidence of the quantitative particle size measurement. As expected, the comparison between specimen preparations of Black2 shows differences in observed particle numbers (Table 2) and differences in the PSDs: the median values of minimum Feret and maximum Feret diameters for grid-on-drop deposition (139 ± 18 nm and 192 ± 17 nm, respectively) are smaller than for drop-on-grid deposition (170 ± 22 nm and 225 ± 20 nm, respectively), even though uncertainty intervals still overlap.

For Red2 and Red3 materials, the quantitative HAADF-STEM analysis was complemented by HAADF-STEM tomography, showing their 3D morphology and the presences of pores. Pore sizes range from 3 to 58 nm in diameter. No differences were observed in pore sizes between the materials. Variations in depth were observed, with some pores crossing the particles entirely (Fig. S.V.2 in supplementary information).

3.5. *Volume specific surface area*

The SSA results range from 5.9 (Black2) to 20.3 m^2/g (Yellow2), with the SSA of red materials ranging from 9.3 (Red3) to 10.8 m^2/g (Red1).

The corresponding VSSA ranges from 30.7 (Black2) to 87.3 m^2/cm^3 (Yellow2) (Table 3).

3.6. Evaluation of organic contamination

PCA of ToF-SIMS mass spectra for the different materials allowed to cluster and separate the samples, and their different forms, based on differences in their surface chemistry, and based on the presence of organic contaminants at trace level. Four principal components (PC) and relative scores were analysed, globally including 97.4% of the dataset variance. Detailed description of the PCA of ToF-SIMS results is provided as supplementary information (Figs. S.VI.1 and S.VI.2). Scores of different samples for the main PC indicate that most of the sample variance can be explained in terms of organic contaminants surface coverage for positive scores (short length aliphatic chains fragments of the form [$C_xH_y^+$]), while negative scores indicated prevalence of an exposed native iron oxide surface chemistry with presence of sodium sulphate compounds. PC2 (σ = 29.7%) was found to be positively correlated with iron (hydr-)oxide clusters ([Fe^+], [$FeOH^+$], [$Fe_xO_y^+$] and [$Fe_xO_yH_z^+$]) and small hydrocarbons ([$C_3H_x^+$], [$C_4H_x^+$]) but negatively correlated to [$NaSO_4^+$] ions and oxidized hydrocarbons [$C_xH_yO^+$]. PC2 scores effectively separates red from yellow E 172 samples. PC3 (σ = 5.7%) was found to be positively correlated with iron ions, iron oxide clusters ([Fe^+], [$Fe_xO_y^+$] and [$Fe_xO_yH_z^+$]), [$NaSO_4^+$] ions and oxidized hydrocarbons [$C_xH_yO^+$] but negatively correlated to iron hydroxide ions, iron oxide clusters ([$FeOH^+$], [$Fe_xO_y^+$] and [$Fe_xO_yH_z^+$]) small hydrocarbons ([$C_3H_x^+$], [C_4H_x]). PC3 separates Black2 and Red3 from the rest of the samples. These results are graphically shown in a PC2-PC3 scores plot (Fig. 5). In general, the data in Fig. 5 cluster the samples according to the [$Fe_xO_y^+$] chemistry (or phase) and qualitatively rank the samples in terms of correlation with contaminants chemistry. Specifically, the top right quadrant correlates with lower level of contamination (from oxidized carbon chains and/or salts) and bottom-left quadrant with higher amount of contamination. Material Red3 is separated from other red materials and from all samples according to presence of both salts and oxidized carbon contamination.

3.7. Evaluation of inorganic contamination

A separate Tof-SIMS data PCA analysis of inorganic peaks revealed the presence of several elemental ions that were also detected at low intensities across different samples and their presence on the surface was qualitatively analysed (Fig. S.VII.1 in supplementary information). The combinations of the first four PC in this case covers 98.3% of the data variance. PC1 with σ = 53.2% essentially separates the samples according to the two main elemental surface contaminants, [Al^+] mainly present in Black2 and [In^+] mainly present in all other cases. PC2 covering 38.3% of the total variance singles out E 172 material Yellow1 according to the presence of, mainly [In^+], [Mn^+], [Mg^+], [As^+]. PC3 and PC4, covering respectively 5.4% and 1.5% of the overall data variance shows the minor contributions of other elemental contaminants in the different samples analysed.

ICP-MS/OES analysis detected concentrations of As, Cr, Ni, Zn, and Al higher than the LOQ in all samples. Values lower than the LOQ were observed in Yellow1 for Cu, in Red1 and Red3 for Pb, and in all samples except Black2 for Cd (Table 4). All measured concentrations are below the upper limits outlined for E 172 in the EU specifications (European Commission, 2012). However, the concentration of Zn in Red2 approached the regulatory limit with the margin of error overlapping the upper limit. Ni reached its highest level in Red1 at 105 mg/kg, while concentrations in other materials remained below 10% of the specification limit. Cr, Cu, and As levels stayed below one-third of their respective specification limits across all samples. Cd and Pb concentrations were at least ten-fold below regulatory thresholds. In Black2 the highest concentrations of Cr, Cu, As, Cd, Pb, and Al were detected, demonstrating markedly elevated levels compared to the red and yellow materials.

STEM-EDX analysis did not demonstrate other inorganic particles than iron (hydr)oxides in any of the examined samples.

3.8. Evaluation of total Fe content

The total mass fraction of Fe in each of the samples was determined by ICP-OES (Table 5). In each sample, the measured concentrations are lower than the nominal concentrations, calculated from the atomic and molecular masses. Furthermore, materials Red1, and Yellow2 have Fe concentrations lower than the minimal Fe concentrations outlined in the EU specifications (European Commission, 2012).

4. Discussion

A detailed physicochemical characterisation of the intrinsic properties of iron (hydr)oxide materials, marketed for use as food additive E 172, was performed in line with the EFSA Guidance on Nanomaterials Risk Assessment (EFSA Scientific Committee et al., 2021) to address some of the existing data gaps for risk assessment highlighted in the

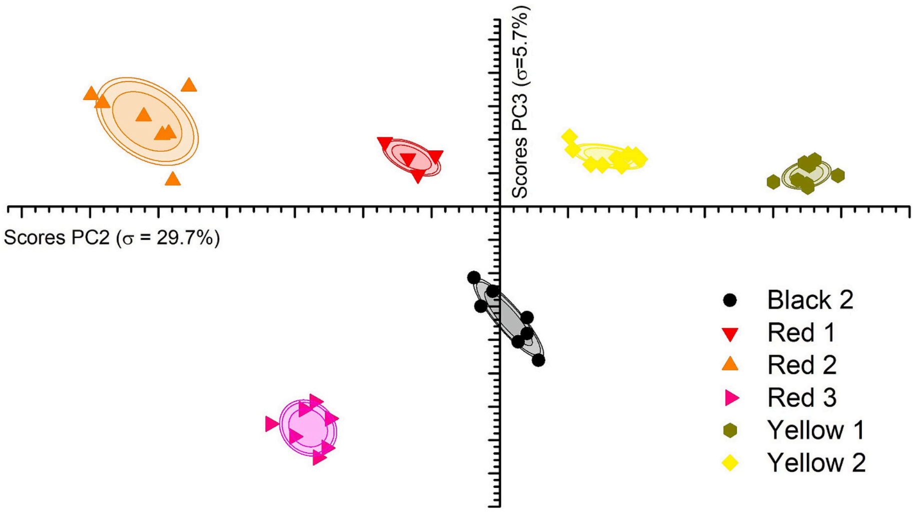

Fig. 5. PCA scores plot for PC2-PC3 resulting from ToF-SIMS mass spectra. Scatter plots represent measurements replicas. Confidence ellipses representing internal sample variability are indicated for 1, 2 and 3-σ standard deviations (*ca.* 68%, 95% and 99.7%, respectively).

Table 4
Mean concentrations of inorganic impurities and combined measurement uncertainties in the materials measured with ICP-MS and ICP-OES.

	Cr	Ni	Cu	Zn	As	Cd	Pb	Al
	mg/kg	mg/kg	mg/kg	mg/kg	mg/kg	mg/kg	mg/kg	mg/kg
Red1	10.4 ± 0.8	105 ± 11	5.3 ± 0.5	2.4 ± 0.2	0.52 ± 0.05	<LOQ	<LOQ	310 ± 40
Red2	8.5 ± 0.7	5.5 ± 0.6	1.48 ± 0.14	94 ± 8	0.78 ± 0.08	<LOQ	0.46 ± 0.05	240 ± 30
Red3	16.5 ± 1.3	11.4 ± 1.2	1.64 ± 0.15	4.5 ± 0.4	0.046 ± 0.005	<LOQ	<LOQ	28 ± 4
Yellow1	2.8 ± 0.3	5.8 ± 0.6	<LOQ	13.5 ± 1.1	0.22 ± 0.03	<LOQ	0.184 ± 0.017	46 ± 6
Yellow2	15.5 ± 1.2	11.6 ± 1.2	1.49 ± 0.14	82 ± 7	0.53 ± 0.05	<LOQ	0.193 ± 0.018	152 ± 19
Black2	31 ± 3	19 ± 2	10.4 ± 1.0	39 ± 4	1.00 ± 0.10	0.067 ± 0.005	0.49 ± 0.05	710 ± 90
LOQ[a]	0.074	0.164	0.245	1.799	0.005	0.050	0.106	8.37
Maximum level[b]	100	200	50	100	3	1	10	not specified

[a] The LOQ was determined by analysing 20 blank samples and determining the deviation between the results, and the combined uncertainty was determined as part of a validation study that included the measurement of spiked samples with known concentrations in triplicate, on three separate days.

[b] As defined in COMMISSION REGULATION (EU) No 231/2012 of 9 March 2012 laying down specifications for food additives listed in Annexes II and III to Regulation (EC) No 1333/2008 of the European Parliament and of the Council.

Table 5
Mean Fe concentrations and standard deviations in the samples measured by ICP-OES.

	Elemental composition	Measured Fe concentration	Nominal Fe concentration	Minimal Fe fraction in specification[a]
		Weight-based fraction	Weight-based fraction	Weight-based fraction
Red1	Fe_2O_3	67.4% ± 0.3%	70%	68%
Red2	Fe_2O_3	68.0% ± 0.7%	70%	68%
Red3	Fe_2O_3	69.3% ± 0.7%	70%	68%
Yellow1	FeO(OH)	61.7% ± 0.2%	63%	60%
Yellow2	FeO(OH)	59.7% ± 1.4%	63%	60%
Black2	Fe_3O_4[b]	70.3% ± 0.5%	72%	68%

[a] As defined in COMMISSION REGULATION (EU) No 231/2012 of 9 March 2012 laying down specifications for food additives listed in Annexes II and III to Regulation (EC) No 1333/2008 of the European Parliament and of the Council.

[b] It was reported during the quantitative EM-analysis that this material consists of Fe_3O_4 with γ-Fe_2O_3 at the surface.

EFSA re-evaluation of 2015 (EFSA Panel on Food Additives and Nutrient Sources added to Food (ANS), 2015). To cover the variety amongst E 172 substances, the analyses were performed on twelve materials from suppliers within and outside of the EU. These materials were marketed as yellow E 172, red E 172, black E 172 or brown E 172, and intended for use within the EU. Based on material colour, phase and particle shape, four main forms were identified: red spheroidal (octahedral) hematite (α-Fe_2O_3); red elongated (rod-like) hematite (α-Fe_2O_3); yellow elongated (rod-like) goethite (α-FeO(OH)); and black spheroidal (cubic) magnetite (Fe_3O_4). These forms correspond with the three substances defined in the EU specifications, based on elemental composition (European Commission, 2012), and two morphologies for red hematite E 172, as already specified in Table 2 of the EFSA 2015 re-evaluation (EFSA Panel on Food Additives and Nutrient Sources added to Food (ANS), 2015). The occurrence of the two morphologies for red hematite E 172 can be related to different production processes: either by calcination of iron hydroxide, either α-FeO(OH) or β-FeO(OH) (Saito et al., 2016; Song et al., 2014), at around 800 °C, or by thermal decomposition of ferrous sulphate heptahydrate, leading to elongated–rod like, referred to as "acicular" in the EFSA 2015 re-evaluation–or spheroidal (octahedral) particle shapes, respectively. The presence of pores in the structure of elongated (rod like) hematite particles has already been described (Echigo et al., 2013; Saito et al., 2016), and is probably due to the calcination process (Saito et al., 2016). A limitation of the present study is that between batch variation could not be determined. Similar observations were made by Voss et al. (Voss, Hsiao, et al., 2020), who also identified hematite, goethite and magnetite for red, yellow, and black E 172, using XRD. However, their E 172 selection did not include a rod-like hematite material, and included one red E 172 material with a different morphology and PSD as to the spheroidal ones analysed in this work.

As opposed to XRD and SAED performing bulk measurements, Raman spectroscopy, and especially XPS, can extract information from the surface of the materials, with a depth of analysis of 5.5–7.5 nm for XPS. They allowed to identify maghemite (γ-Fe_2O_3) as the dominant phase at the surface of the magnetite (Fe_3O_4) particles. Both maghemite (γ-Fe_2O_3) and hematite (α-Fe_2O_3) are polymorphs of Fe_2O_3 and exhibit a similar red hue when in their pristine powder form, but maghemite has a similar inverse spinel crystal structure as magnetite (Fe_3O_4) (Cornell & Schwertmann, 2003a). Maghemite is known to be a weathering product of magnetite (Cornell & Schwertmann, 2003c), and for material Black2, the maghemite at the surface can be present, *e.g.*, as a result of the production process or of post-production weathering. To our knowledge, pure maghemite materials are sold outside of the EU for food applications (Iron Oxide Red Magnetic 12 Oz Total (4 Bottles) USP Food Grade 44 Micron Powder, *n.d.*; Red Magnetic Iron Oxide [y-Fe2O3] 90% USP Food Grade Powder 1.1 Lb in 3 Bottles, *n.d.*) but we could not purchase them within the EU. Although the EFSA 2015 re-evaluation do not mention maghemite as a food additive (EFSA Panel on Food Additives and Nutrient Sources added to Food (ANS), 2015) and the EU specifications of the different E 172 iron (hydr)oxides does not explicitly specify their crystal structure (European Commission, 2012), the finding that maghemite is present at the surface of magnetite used as food additive deserves consideration in the risk assessment of these substances.

Amongst the twelve E 172 materials, four mixtures were identified consisting of a combination of several E 172 forms. This was expected for brown E 172, a known blend of the different iron (hydr)oxides) (EFSA Panel on Food Additives and Nutrient Sources added to Food (ANS), 2015; European Commission, 2012). Two samples advertised as black E 172 were also shown to be mixtures of different forms (blending of magnetite and goethite). This indicates that a variety of particle combinations might be present on the market, which are not always sold as brown E 172. The EU specifications already specified that a range of hues including yellows, reds, browns and blacks is applied, and Voss et al. showed that pigment(s) with an orange hue consist of a mixture composed of goethite and hematite (Voss, Hsiao, et al., 2020).

When dispersed at neutral pH in MilliQ water, the zeta potential values of all E 172 materials, except Red3, lie between −30 mV and +30 mV, indicating low dispersion stability. This was substantiated by the observed precipitation for all materials under these conditions, possibly explaining the large (agglomerate) particle sizes measured by dynamic light scattering (DLS) and laser diffraction (LD), reported in the EFSA 2015 re-evaluation (EFSA Panel on Food Additives and Nutrient Sources added to Food (ANS), 2015). To improve the stability of the dispersions, the generic NANOGENOTOX protocol was applied (Jensen et al., 2011), providing electrosterical stabilisation. The NANOGENOTOX protocol, including the amendments as established in NANoREG (Booth & Jensen, 2015), was demonstrated to be a suitable dispersion protocol for dispersing the yellow and red E 172 materials since dispersions remained stable for at least 1 h based on visual inspection, and it allowed reliable measurements of the PSD using EM. Quantitative HAADF-STEM analysis resulted in median values of the minimum Feret diameter distributions of 88 ± 11 nm (Red1), 88 ± 16 (Red2) and 106 ± 19 nm (Red3) for red E 172 materials; and between 72 ± 13 nm (Yellow2) and 96 ± 17 nm (Yellow1) for yellow E 172 materials. Voss et al. reported comparable median values of 82 nm for octahedral red E 172, and a range between 62 and 79 nm for yellow E 172 materials (Voss, Hsiao, et al., 2020). Voss et al. observed nanostructures in black E 172 materials, but could not provide quantitative TEM analysis results (Voss, Hsiao, et al., 2020), and determined a median particle size of 54 nm by small-angle X-ray scattering (SAXS). However, in a regulatory context, SAXS is regarded as a screening method, contrary to EM which is considered a confirmatory method. SAXS can lead to underestimation of the median particle size for materials with a broad PSD, a median particle size above 100 nm, and/or with an elongated morphology (European Commission: Joint Research Centre et al., 2020; Rauscher et al., 2023). It is unclear if the black E 172 material described by Voss et al. has different properties than the one analysed in this study (Black2) or if the difference is method-dependent.

For materials that remain stable in dispersion, similar particle size distributions are expected when applying either grid-on-drop or drop-on-grid sampling approaches. However, in the case of Black2, the strong magnetic interactions unavoidably results in agglomeration and sedimentation of particles, which hinders preparation of a stable dispersion and sample preparation for EM particle sizing. Only the fraction of particles that remains in dispersion is retained on the grid when the grid-on-drop approach is applied. The amount of sampled particles is very low, making the resulting size distribution less reliable (Fig. S.II.2). Applying the drop-on-grid approach leads to an overloaded grid covered with large agglomerates, for which accurate measurement of constituent particle size becomes difficult due to strong particle overlap (Fig. S.II.2). Even though these methodological differences are reflected in the different median values for minimum and maximum Feret diameters obtained for grid-on-drop (minimum Feret diameter: 139 ± 18, maximum Feret diameter: 192 ± 17 nm) and drop-on-grid (minimum Feret diameter: 170 ± 22 nm, maximum Feret diameter: 225 ± 20 nm) depositions, the size distributions of the constituent particles obtained by both sampling approaches are in fact still broadly comparable as indicated by the overlapping uncertainty intervals of the median values, and the comparable interquartile ranges (D75-D25) (minimum Feret diameter: 84 nm (grid-on-drop) *vs* 93 nm (drop-on-grid); maximum Feret diameter: 114 nm (grid-on-drop) *vs* 135 nm (drop-on-grid)). Even though there are limitations of the applied sampling approaches to determine the PSD of Black2 accurately, they are well suited to identify the smallest particles present in the material (D10 of minimum Feret diameter is 79 nm for grid-on-drop and 94 nm for drop-on-grid), as the bias is expected towards the largest particles/agglomerates that sediment faster. Importantly, both approaches consistently demonstrate the presence of a substantial fraction of particles below 250 nm of the fraction below 500 nm (91% for grid-on-drop; 86% for drop-on-grid). Therefore the identification and sizing of the smallest particle fraction is considered to be robust, whereas the relative contribution of larger particles is associated with higher uncertainty. In accordance with EFSA Guidance on Particle Technical Requirements, this finding implies that the EFSA Guidance on Nanomaterials Risk Assessment should be applied, independent of uncertainties in the exact numerical nano-fraction. Finally, the inability to obtain stable dispersions for Black2 is not only a methodological limitation for PSD analysis, but also represents a relevant challenge for *in vitro* testing, where dispersion stability is a critical prerequisite. This aspect further underscores the importance of detailed physicochemical characterisation when assessing the suitability of such materials for risk assessment–relevant testing.

The observed D10 value of the minimum Feret diameter of 79 ± 23 nm suggests that Black2 does not contain particles in the size range of superparamagnetic iron oxide nanoparticles (SPIONS). SPIONS are maghemite or magnetite particles smaller than ~25 nm, which have different magnetic properties and are often used for biomedical applications (Baabu et al., 2022). Moreover, SPIONS often have an organic surface coating present to increase their biocompatibility. The presence of an organic coating is generally considered not to be used in E 172 in marketed food (EFSA Panel on Food Additives and Nutrient Sources added to Food (ANS), 2015) and is not mentioned in the 2015 re-evaluation of E 172, either. Ion release in acidic pH, intracellular uptake, oxidative stress induction and, in some cases, genotoxicity have been demonstrated for both maghemite and magnetite SPIONs, observed depending on the size and surface coating of the particles (Ahamed et al., 2013; Evans et al., 2019; Pöttler et al., 2015; Singh et al., 2012; Wu et al., 2022).

The magnification selected for the quantitative HAADF-STEM analysis ensured that more than 95% of the minimum Feret diameter measurements are between the LLOQ and the ULOQ. This magnification leads to a large fraction of particles with a maximum Feret diameter above the ULOQ for rod-like E 172 materials (55%–75%). In this case, combining the systematic random sampling with a stage shift centring the particles of interest allowed to limit biased measurement of the maximum external dimension by avoiding overlap of the particles and the measurement frame. The quantitative HAADF-STEM analysis showed that all analysed materials contain a fraction of particles smaller than 250 nm. From the fraction of particles smaller than 500 nm, the percentage of particles below 250 nm ranges from 86% to 100% for the different materials. These findings indicate, that nano-specific properties need to be considered in the risk assessment of E 172, in line with the EFSA Guidance on Particle Technical Requirements (EFSA Scientific Committee et al., 2021).

BET measurements of red E 172 materials resulted in a VSSA in line with literature data of E 172: less variation was observed for our red E 172 materials (49.3 to 56.8 m^2/cm^3), compared to the literature (13.1 to 64.9 m^2/cm^3, and 21.0 to 91.0 m^2/cm^3) (Venator, 2019; Voss, Hsiao, et al., 2020). The smallest VSSA obtained by Voss et al. corresponds to the red E 172 material with a different morphology, not analysed in this work. The VSSA of Yellow2 (86.2 m^2/cm^3) is slightly above the ranges reported in the literature (55.7 to 70.9 m^2/cm^3, and 71.9 to 77.0 m^2/cm^3), while the VSSA of Black2 (30.6 m^2/cm^3) is within the ranges (26.5 to 73.8 m^2/cm^3, and 26.9 to 49.6 m^2/cm^3) (Venator, 2019; Voss, Hsiao, et al., 2020). The Commission recommendation on the definition of nanomaterial specifies that the NanoDefine project demonstrated that there were no inconsistencies in classification of non-nanomaterials based on the VSSA being less than 6 m^2/cm, a material is not considered a nanomaterial if its VSSA is smaller than 6 m^2/cm^3 (European Commission, 2022; European Commission: Joint Research Centre et al., 2020). For the analysed materials, VSSA values were all above 6 m^2/cm^3. Based on the flowchart by Rauscher et al. (Rauscher et al., 2023), additional confirmatory testing is required for materials with VSSA above 6 m^2/cm^3. HAADF-STEM analyses indicated that Red1, Red2, Yellow1 and Yellow2 have a median minimum Feret diameter just below 100 nm, while for Red3 and Black2 the medians are above 100 nm. Even so, for most materials, the expended uncertainty intervals extend beyond the 100 nm size limit, making classification following the 2022 EC Recommended definition complex. Additional bias resulting from sampling and/or image analysis cannot be completely excluded. Moreover, because the applicable definition of a nanomaterial in the context of food requires that the material is an “engineered nanomaterial” (European Commission, 2015), which is intentionally produced, information of the PSD alone will, however, not allow to define the material as a nanomaterial because intentionality cannot be demonstrated from the PSD.

ToF-SIMS allowed to discriminate the samples, and their different forms, based on differences in their surface chemistry and on the presence of organic contaminants at trace level. Although short aliphatic carbon molecules are likely present as contaminants in the samples, a certain base level cannot be avoided from sample manipulation during storage, transport and preparation. A baseline level is therefore expected in all samples. Oxidized carbon chains, [$C_xH_yO^+$], are more likely originating from the sample itself, as their baseline level from adventitious contamination can be considered very low. Surfactants like oleic acid are also sometimes added on the surface post-synthesis to stabilize the nanoparticles in solution, and these or similar molecules could be at the origin of the observed organic ions fragments. Other impurities, such as Na or S containing compounds, are very likely originating from the material synthesis (wet process or introduced as counter ions). ToF-SIMS data showed more impurities for the Red3 material. This presence of other components in Red3 could explain the different zeta potential curve obtained for this material compared to the other E 172 materials.

The quantification of inorganic contamination was difficult using the SIMS technique due to ionization cross section and matrix effects dependence of mass spectral intensities, but their presence on the surface of different samples could be qualitatively analysed, indicating presence of Al, In, Mg, Mn and As. AlO_x and In are used as support material and catalyst promoters in FeO_x mediated hydrocarbon synthesis (Chaudhari et al., 2024; Liu et al., 2022) and their presence could be originating from production line trace contaminations. Mn and Mg are again used as dopant for specific applications (Hornak, 2021; Yadav et al., 2023), while the presence of As could be the result of chemisorption process from H_2O during wet synthesis process, due to its strong affinity with iron oxides (Torasso et al., 2023).

ICP-OES results demonstrate that all materials contain a lower fraction of Fe than would be theoretically expected based on the molecular composition of the pure materials. Materials Red1 and Yellow2 exhibit Fe concentrations below the minimum Fe concentrations specified in the EU specifications (European Commission, 2012). Nevertheless, when an extended uncertainty, calculated as 2 or 3 times the relative standard deviation, is considered, there is overlap with the values outlined in the specifications. Consequently, the measurement uncertainty associated with ICP-OES determination of total Fe cannot reliably distinguish the relatively small amounts of Na- or S-containing compounds.

The measured concentrations of other inorganic contaminants align with the findings of Voss et al., showing comparable orders of magnitude for Cr (2.0–35 mg/kg), Ni (3.1–60 mg/kg), Cu (<LOQ–2.8 mg/kg), Zn (43–277 mg/kg), As (0.1–0.6 mg/kg), and Cd (<LOQ–0.1 mg/kg). Notably, the current study demonstrates lower Pb concentrations (<LOQ–0.49 mg/kg) compared to those reported by Voss et al. (Voss, Hsiao, et al., 2020) (0.5–2.7 mg/kg). The findings confirm that certain toxic elements (Cr, Cu, As, Cd, and Pb) are present at concentrations several-fold lower than regulatory specification limits. Nickel and Zn are present close below specification limits. The variations in inorganic contamination levels, observed amongst different E 172 materials reflect differences in synthesis processes and raw material sources used in manufacturing the various materials. Colour-dependent contamination patterns emerged from the analysis. Consistent with Voss et al. (Voss, Hsiao, et al., 2020), the highest concentrations of Cr and Pb were detected in the black material. However, our study revealed a broader contamination profile in the black material, with elevated levels of Cu, As, and Cd that were not observed in the previous study, where these elements remained within the concentration ranges of other colours. The elevated Al content of 710 mg/kg detected in the black material (compared with a range of 28–310 mg/kg in the other materials) may result from the intentional addition of aluminium compounds during production to achieve the desired colour characteristics, representing a process-related rather than contamination-based source of this element. Ultimately, because these trace elements consistently remain below regulatory limits and represent a small fraction of total exposure, a detailed chronic safety discussion for these impurities would not significantly alter the risk assessment of E 172. This is supported by Kennedy et al. (Kennedy et al., 2020), who emphasise that cumulative risk assessment applied to all possible substance combinations is impractical and highly inefficient and that efforts should rather be targeted at substances for which the potential contribution to risk is the greatest.

It remains to be determined whether the observed differences in crystal structure, oxidation state, and surface chemistry of the various E 172 forms can be linked to differences in toxicity. The difference between magnetite and maghemite may, for example, be particularly relevant in the context of gastrointestinal exposure following oral intake, as the presence of Fe(II) in magnetite confers higher redox activity compared with fully oxidized maghemite, which may influence surface reactivity under the variable pH and redox conditions encountered along the gastrointestinal tract. Beyond redox potential, morphology can impacts behaviour. A higher dissolution rate was found for hematite obtained by calcination of goethite, *i.e.* elongated with pores, compared to solution-grown hematite, *i.e.* spheroidal (Cornell & Schwertmann, 2003b). Therefore, the porosity of elongated hematite particles could potentially affect dissolution kinetics as the porosity of the material contributes to a higher interaction with digestive fluids. Li et al. have shown that the pore size in the material increases after 4 h during gastric *in vitro* digestion (Li et al., 2023). However, the dissolution of iron oxides within the gastrointestinal tract is a process governed by multiple parameters, *e.g.* surface chemistry or agglomeration state, and its porosity alone cannot be directly linked to increased bioavailability without more dedicated dissolution or *in vitro* digestion studies performed on both forms of hematite.

Following ECHA, EFSA, and OECD regulatory and guidance documents, grouping and read-across of substances must be endpoint-specific and depends on the physicochemical properties of the source and target materials (EFSA Scientific Committee et al., 2025; European Commission, 2006; OECD, 2025). However, similarity in size or composition between substances are not sufficient criteria for grouping, and properties such as dissolution rate, surface chemistry or morphology have to be taken into account depending on the endpoint. The results of this study suggests that grouping of E 172 substances is not advisable for risk assessment due to the variation of their physicochemical properties, including intra-substance variability (2 forms of red E 172, maghemite on surface magnetite). This should be considered at the level of specification of the food additive and for its risk assessment.

In conclusion, this work performed a detailed physicochemical characterisation of the intrinsic properties of iron (hydr)oxides applied as food additive E 172 and can contribute to fill the data gaps identified by the EFSA 2015 re-evaluation. It provides insight into the distinct E 172 forms and possibilities for read-across. The results are useful for the follow-up assessment of E 172 by the EU program for the re-evaluation of food additives (Food Improvement Agents—Food Additives (EFSA-Q-2021-00178, Status: Ongoing Risk Assessment), 2025), and it will support the development of standardised characterisation protocols for food-grade particulate materials in the context of risk assessment and control programs.

CRediT authorship contribution statement

Lisa Siciliani: Writing – review & editing, Writing – original draft, Visualization, Validation, Software, Methodology, Investigation, Formal analysis, Data curation, Conceptualization. **Francesco Fumagalli:** Writing – review & editing, Visualization, Validation, Resources, Investigation. **Jessica Ponti:** Writing – review & editing, Validation, Resources, Investigation, Conceptualization. **Alessia Bogni:** Writing – review & editing, Validation, Investigation. **Linde Sevenants:** Writing – review & editing. **Dario Geebelen:** Writing – review & editing. **Noa Olluyn:** Writing – review & editing, Validation, Investigation. **Daniela Montalvo:** Writing – review & editing, Visualization, Investigation. **Karlien Cheyns:** Writing – review & editing, Investigation. **Charlotte Wouters:** Writing – review & editing. **Jan Mast:** Writing – review &

editing, Supervision, Software, Project administration, Funding acquisition. **Nathalie Claes:** Writing – review & editing, Visualization, Investigation. **Sara Bals:** Writing – review & editing, Supervision, Resources, Conceptualization. **Eveline Verleysen:** Writing – review & editing, Visualization, Validation, Supervision, Resources, Project administration, Methodology, Investigation, Funding acquisition, Formal analysis, Data curation, Conceptualization.

Funding sources

This research is part of the NAMs4NANO Project 'Integration of New Approach Methodologies results in chemical risk assessments: Case studies addressing nanoscale considerations' (GP/EFSA/MESE/2022/01) funded by the European Food Safety Authority (EFSA). The views expressed in this communication are solely those of the author, and EFSA does not assume responsibility for any application or interpretation of the information provided herein.

Declaration of competing interest

The authors declare that they have no known competing financial interests or personal relationships that could have appeared to influence the work reported in this paper.

Acknowledgements

The authors would like to acknowledge the contribution of Frederic Van Steen and Khariklia Tsilikas to sample preparation and image analysis.

Appendix A. Supplementary data

Supplementary data to this article can be found online at https://doi.org/10.1016/j.fochx.2026.104064.

Data availability

The authors do not have permission to share data.

References

van Aarle, W., Palenstijn, W. J., Cant, J., Janssens, E., Bleichrodt, F., Dabravolski, A., … Sijbers, J. (2016). Fast and flexible X-ray tomography using the ASTRA toolbox. *Optics Express, 24*(22), 25129–25147. https://doi.org/10.1364/OE.24.025129

van Aarle, W., Palenstijn, W. J., De Beenhouwer, J., Altantzis, T., Bals, S., Batenburg, K. J., & Sijbers, J. (2015). The ASTRA Toolbox: A platform for advanced algorithm development in electron tomography. *Ultramicroscopy, 157*, 35–47. https://doi.org/10.1016/j.ultramic.2015.05.002

Ahamed, M., Alhadlaq, H. A., Alam, J., Majeed Khan, M. A., Ali, D., & Alarafi, S. (2013). Iron oxide nanoparticle-induced oxidative stress and genotoxicity in human skin epithelial and lung epithelial cell lines. *Current Pharmaceutical Design, 19*(37), 6681–6690. https://doi.org/10.2174/1381612811319370011

Artusio, F., Fumagalli, F., Valsesia, A., Ceccone, G., & Pisano, R. (2021). Role of self-assembled surface functionalization on nucleation kinetics and oriented crystallization of a small-molecule drug: batch and thin-film growth of aspirin as a case study. *ACS Applied Materials & Interfaces, 13*(13), 15847–15856. https://doi.org/10.1021/acsami.1c00460

Baabu, P. R. S., Kumar, H. K., Gumpu, M. B., Babu, K. J., Kulandaisamy, A. J., & Rayappan, J. B. B. (2022). Iron oxide nanoparticles: A review on the province of its compounds, properties and biological applications. *Materials, 16*(1), 59. https://doi.org/10.3390/ma16010059

Bañuls-Ciscar, J., Fumagalli, F., Ruiz-Moreno, A., Rossi, F., Suraci, S. V., Fabiani, D., & Ceccone, G. (2020). A methodology to investigate heterogeneous oxidation of thermally aged cross-linked polyethylene by ToF-SIMS. *Surface and Interface Analysis, 52*(12), 1178–1184. https://doi.org/10.1002/sia.6848

Bennet, F., Müller, A., Radnik, J., Hachenberger, Y., Jungnickel, H., Laux, P., Luch, A., & Tentschert, J. (2020). Preparation of nanoparticles for ToF-SIMS and XPS analysis. *Journal of Visualized Experiments: JoVE, 163*. https://doi.org/10.3791/61758

Bennet, F., Opitz, R., Ghoreishi, N., Plate, K., Barnes, J.-P., Bellew, A., … Radnik, J. (2023). VAMAS TWA2 interlaboratory comparison: Surface analysis of TiO2 nanoparticles using ToF-SIMS. *Journal of Vacuum Science & Technology A, 41*(5), Article 053210. https://doi.org/10.1116/6.0002814

BfR Recommendations on Food Contact Materials—BfR. August 13) https://www.bfr.bund.de/en/bfr_recommendations_on_food_contact_materials-1711.html, (2025).

Biesinger, M. C., Payne, B. P., Grosvenor, A. P., Lau, L. W. M., Gerson, A. R., Smart, R. S., & C.. (2011). Resolving surface chemical states in XPS analysis of first row transition metals, oxides and hydroxides: Cr, Mn, Fe, Co and Ni. *Applied Surface Science, 257*(7), 2717–2730. https://doi.org/10.1016/j.apsusc.2010.10.051

Booth, A., & Jensen, K. A. (2015). NANoREG D4. 12 SOP Probe Sonicator Calibration for Ecotoxicological Testing. , January 15 https://www.rivm.nl/en/documenten/nanoreg-d212-dr-framework-and-procedures-for-characterization-and-reporting-of.

Braniste, T., Dragoman, M., Zhukov, S., Aldrigo, M., Ciobanu, V., Iordanescu, S., Alyabyeva, L., Fumagalli, F., Ceccone, G., Raevschi, S., Schütt, F., Adelung, R., Colpo, P., Gorshunov, B., & Tiginyanu, I. (2020). Aero-Ga2O3 nanomaterial electromagnetically transparent from microwaves to terahertz for internet of things applications. *Nanomaterials, 10*(6), Article 6. https://doi.org/10.3390/nano10061047

Bresch, H., Hodoroaba, V.-D., Schmidt, A., Rasmussen, K., & Rauscher, H. (2022). Counting small particles in electron microscopy images—Proposal for rules and their application in practice. *Nanomaterials, 12*(13), Article 13. https://doi.org/10.3390/nano12132238

CFR—Code of Federal Regulations Title 21. Part 186—Indirect Food Substances Affirmed as Generally Recognized as Safe—Ferric Oxide (21 CFR 186.1300) (2018). https://www.ecfr.gov/current/title-21/part-73.

CFR—Code of Federal Regulations Title 21. Part 186—Indirect Food Substances Affirmed as Generally Recognized as Safe—Iron Oxides (21 CFR 186.1374) (2018). https://www.ecfr.gov/current/title-21/part-73.

CFR—Code of Federal Regulations Title 21. Part 73—Listing of Color Additives Exempt from Certification—Synthetic Iron Oxide (21 CFR 73.200) (2018). https://www.ecfr.gov/current/title-21/part-73.

Chaudhari, D. S., Upadhyay, R. P., Shinde, G. Y., Gawande, M. B., Filip, J., Varma, R. S., & Zbořil, R. (2024). A review on sustainable iron oxide nanoparticles: Syntheses and applications in organic catalysis and environmental remediation. *Green Chemistry, 26*(13), 7579–7655. https://doi.org/10.1039/D4GC01870B

Cornell, R. M., & Schwertmann, U. (2003). Crystal Structure. In *The iron oxides: Structure, properties, reactions, occurrences and uses* (pp. 9–38). John Wiley & Sons, Ltd.. https://doi.org/10.1002/3527602097.ch2

Cornell, R. M., & Schwertmann, U. (2003). Dissolution. In *The iron oxides: Structure, properties, reactions, occurrences and uses* (pp. 297–344). John Wiley & Sons, Ltd.. https://doi.org/10.1002/3527602097.ch12

Cornell, R. M., & Schwertmann, U. (2003). Introduction to the iron oxides. In *The iron oxides: Structure, properties, reactions, occurrences and uses* (pp. 1–7). John Wiley & Sons, Ltd.. https://doi.org/10.1002/3527602097.ch1

ECHA. (2022). Appendix for nanoforms to the guidance on registration and the guidance on substance identification: Version 2.0 January 2022. https://doi.org/10.2823/40.

Echigo, T., Monsegue, N., Aruguete, D. M., Murayama, M., & Hochella, M. F. (2013). Nanopores in hematite (α-Fe2O3) nanocrystals observed by electron tomography. *American Mineralogist, 98*(1), 154–162. https://doi.org/10.2138/am.2013.4120

EFSA Panel on Additives and Products or Substances used in Animal Feed (FEEDAP). (2016). Safety and efficacy of iron oxide black, red and yellow for all animal species. *EFSA Journal, 14*(6), Article e04482. https://doi.org/10.2903/j.efsa.2016.4482

EFSA Panel on Food Additives and Nutrient Sources added to Food (ANS). (2015). Scientific Opinion on the re-evaluation of iron oxides and hydroxides (E 172) as food additives. *EFSA Journal, 13*(12), 4317. https://doi.org/10.2903/j.efsa.2015.4317

EFSA Panel on Food Contact Materials, Enzymes, Flavourings and Processing Aids (CEF). (2013). Scientific Opinion on the safety assessment of the active substances iron, iron oxides, sodium chloride and calcium hydroxide for use in food contact materials. *EFSA Journal, 11*(10), 3387. https://doi.org/10.2903/j.efsa.2013.3387

EFSA Scientific Committee, Bennekou, S. H., Allende, A., Bearth, A., Casacuberta, J., Castle, L., … Serafimova, R. (2025). Guidance on the use of read-across for chemical safety assessment in food and feed. *EFSA Journal, 23*(7), Article e9586. https://doi.org/10.2903/j.efsa.2025.9586

EFSA Scientific Committee, More, S., Bampidis, V., Benford, D., Bragard, C., Halldorsson, T., … Schoonjans, R. (2021). Guidance on technical requirements for regulated food and feed product applications to establish the presence of small particles including nanoparticles. *EFSA Journal, 19*(8), Article e06769. https://doi.org/10.2903/j.efsa.2021.6769

EFSA Scientific Committee, More, S., Bampidis, V., Benford, D., Bragard, C., Halldorsson, T., Hernández-Jerez, A., Hougaard Bennekou, S., Koutsoumanis, K., Lambré, C., Machera, K., Naegeli, H., Nielsen, S., Schlatter, J., Schrenk, D., Silano, V., Turck, D., Younes, M., Castenmiller, J., … Schoonjans, R. (2021). Guidance on risk assessment of nanomaterials to be applied in the food and feed chain: Human and animal health. EFSA Journal, *19*(8), 6768, 111. https://doi.org/https://doi.org/10.2903/j.efsa.2021.6768.

European Commission. (2006). Regulation (EC) No 1907/2006 of the European Parliament and of the Council of 18 December 2006 concerning the Registration, Evaluation, Authorisation and Restriction of Chemicals (REACH), establishing a European Chemicals Agency, amending Directive 1999/45/EC and repealing Council Regulation (EEC) No 793/93 and Commission Regulation (EC) No 1488/94 as well as Council Directive 76/769/EEC and Commission Directives 91/155/EEC, 93/67/EEC, 93/105/EC and 2000/21/EC. *Official Journal of the European Union, 49*(L 396), 1–849.

European Commission. (2008). Regulation (EC) No 1333/2008 of the European Parliament and of the Council of 16 December 2008 on food additives (Text with EEA relevance). *Official Journal of the European Union, 51*(L354), 16–33.

European Commission. (2011). Commission Regulation (EU) No 10/2011 of 14 January 2011 on plastic materials and articles intended to come into contact with food. *Official Journal of the European Union, 54*(L12), 1–89.

European Commission. (2012). Commission Regulation (EU) No. 231/2012 of 9 March 2012 laying down specifications for food additives listed in Annexes II and III to Regulation (EC) No. 1333/2008 of the European Parliament and of the Council. *Official Journal of the European Union, 55*(L83), 1–295.

European Commission. (2015). Regulation (EU) 2015/2283 of the European Parliament and of the Council of 25 November 2015 on Novel Foods, Amending Regulation (EU) No 1169/2011 of the European Parliament and of the Council and repealing Regulation (EC) No 258/97 of the European Parliament and of the Council and Commission Regulation (EC) No 1852/2001. *Official Journal of the European Union, 58*(L 327), 1–22.

European Commission. (2022). Commission Recommendation of 10 June 2022 on the definition of nanomaterial 2022/C 229/01. *Official Journal of the European Union, 65* (C 229), 1–5.

European Commission: Joint Research Centre, Mech, A., Rauscher, H., Babick, F., Hodoroaba, V., Ghanem, A., … Gilliland, D. (2020). The NanoDefine methods manual – 2020. *Publications Office of the European Union.*. https://doi.org/10.2760/79490

Evans, S. J., Clift, M. J. D., Singh, N., Wills, J. W., Hondow, N., Wilkinson, T. S., … Doak, S. H. (2019). In vitro detection of in vitro secondary mechanisms of genotoxicity induced by engineered nanomaterials. *Particle and Fibre Toxicology, 16* (1), 8. https://doi.org/10.1186/s12989-019-0291-7

Fairley, N., Fernandez, V., Richard-Plouet, M., Guillot-Deudon, C., Walton, J., Smith, E., Flahaut, D., Greiner, M., Biesinger, M., Tougaard, S., Morgan, D., & Baltrusaitis, J. (2021). Systematic and collaborative approach to problem solving using X-ray photoelectron spectroscopy. Applied Surface Science Advances, 5, 100112. https://doi.org/https://doi.org/10.1016/j.apsadv.2021.100112.

Favela-Camacho, S. E., Samaniego-Benítez, E. J., Godínez-García, A., Avilés-Arellano, L. M., & Pérez-Robles, J. F. (2019). How to decrease the agglomeration of magnetite nanoparticles and increase their stability using surface properties. *Colloids and Surfaces A: Physicochemical and Engineering Aspects, 574*, 29–35.

Food Improvement Agents—Food Additives (EFSA-Q-2021-00178, Status: Ongoing Risk Assessment). , February 21 https://open.efsa.europa.eu/questions/EFSA-Q-2021-00178, (2025).

Freedman, D., & Diaconis, P. (1981). On the histogram as a density estimator: L2 theory. *Zeitschrift Für Wahrscheinlichkeitstheorie Und Verwandte Gebiete, 57*(4), 453–476. https://doi.org/10.1007/BF01025868

Hornak, J. (2021). Synthesis, properties, and selected technical applications of magnesium oxide nanoparticles: A review. *International Journal of Molecular Sciences, 22*(23), Article 23. https://doi.org/10.3390/ijms222312752

Iron Oxide Red Magnetic 12 Oz Total (4 Bottles) USP Food Grade 44 Micron Powder. (n.d.). eBay. Retrieved June 2, 2025, from https://www.ebay.com/itm/202953602232.

Jain, A., Ong, S. P., Hautier, G., Chen, W., Richards, W. D., Dacek, S., … Persson, K. A. (2013). Commentary: The Materials Project: A materials genome approach to accelerating materials innovation. *APL Materials, 1*(1), Article 011002. https://doi.org/10.1063/1.4812323

JECFA. (1980). *Twenty-third report of the Joint FAO/WHO Expert Committee on evaluation of certain food additives*. WHO Technical Report Series, No 648.

JECFA. (2008). *Compendium of food additive specifications*. FAO JECFA Monographs Series, No 5.

Jensen, K. A., Clausen, P. A., Birkedal, R., Kembouche, Y., Christiansen, E., Jacobsen, N. R., … Wallin, H. (2011). *The generic NANOGENOTOX dispersion protocol—Standard operating procedures for characterization of the selected manufactured nanomaterials types*. Deliverable Report No. 3.

JRC Nanomaterials Repository—European Commission. (n.d.). Retrieved July 16, 2025, from https://joint-research-centre.ec.europa.eu/scientific-tools-and-databases-0/jrc-nanomaterials-repository_en.

Kennedy, M. C., Hart, A. D. M., Kruisselbrink, J. W., van Lenthe, M., de Boer, W. J., van der Voet, H., … van Klaveren, J. (2020). A retain and refine approach to cumulative risk assessment. *Food and Chemical Toxicology, 138*, Article 111223. https://doi.org/10.1016/j.fct.2020.111223

Li, J., Wang, L., Li, S., Liang, X., Zhang, Y., Wang, Y., & Liu, Y. (2023). Sustained oral intake of nano-iron oxide perturbs the gut-liver axis. *NanoImpact, 30*, Article 100464. https://doi.org/10.1016/j.impact.2023.100464

Liu, J., Li, B., Cao, J., Song, C., & Guo, X. (2022). Effects of indium promoter on iron-based catalysts for CO2 hydrogenation to hydrocarbons. *Journal of CO2 Utilization, 65*, Article 102243. https://doi.org/10.1016/j.jcou.2022.102243

Mast, J., De Temmerman, P.-J., Witschger, O., Bau, S., Francis, L., Galvao, P., Lloris, J. M., Sabella, S., Pompa, P., Valentini, P., Rissler, J., Pagels, J., Motzkus, C., Mace, T., Pozzi Mucelli, S., Micheletti, C., Oughton, D., Lind, O.-C., & Jensen, K. A. (2015, October 15). NANoREG D2.10 SOP 01 Preparation of EM-grids containing a representative sample of a dispersed NM. https://www.rivm.nl/en/documenten/nanoreg-d210-sop-01-preparation-of-em-grids-containing-representative-sample-of.

Nanotechnologies - Guidance on Detection and Identification of Nano-Objects in Complex Matrices, CEN/TS 17273:2018 (2018). https://standards.iteh.ai/catalog/standards/cen/09a8f405-5b24-40e5-82e2-256c5caef495/cen-ts-17273-2018.

OECD. (2025). *Guidance on grouping of chemicals, Third Edition (No. 418; OECD Series on Testing and Assessment 418)*. OECD Publishing. https://doi.org/10.1787/b254a158-en.

Particle Size Analysis — Image Analysis Methods — Part 1: Static Image Analysis Methods. (2014). *ISO 13322-1:2014*.

Pöttler, M., Staicu, A., Zaloga, J., Unterweger, H., Weigel, B., Schreiber, E., Hofmann, S., Wiest, I., Jeschke, U., Alexiou, C., & Janko, C. (2015). Genotoxicity of superparamagnetic iron oxide nanoparticles in granulosa cells. *International Journal of Molecular Sciences, 16*(11), 26280–26290. https://doi.org/10.3390/ijms161125960

Rauscher, H., Kestens, V., Rasmussen, K., Linsinger, T. P. J., & Stefaniak, E. (2023). *Guidance on the implementation of the Commission Recommendation 2022/C 229/01 on the definition of nanomaterial (Scientific Analysis or Review KJ-NA-31-452-EN-N (online),KJ-NA-31-452-EN-C (print))*. Publications Office of the European Union. https://doi.org/10.2760/143118%20(online),10.2760/237496%20(print).

Red Magnetic Iron Oxide [y-Fe2O3] 90% USP Food Grade Powder 1.1 Lb in 3 Bottles. (n.d.). eBay. Retrieved June 2, 2025, from https://www.ebay.com/itm/223829773073.

Saito, G., Nomura, T., Sakaguchi, N., & Akiyama, T. (2016). Optimization of the dehydration temperature of goethite to control pore morphology. *ISIJ International, 56*(9), 1598–1605. https://doi.org/10.2355/isijinternational.ISIJINT-2016-231

Schindelin, J., Arganda-Carreras, I., Frise, E., Kaynig, V., Longair, M., Pietzsch, T., … Cardona, A. (2012). Fiji: An open-source platform for biological-image analysis. *Nature Methods, 9*(7), 676–682. https://doi.org/10.1038/nmeth.2019

Sieg, H., Schaar, C., Fouquet, N., Böhmert, L., Thünemann, A. F., & Braeuning, A. (2024). Particulate iron oxide food colorants (E 172) during artificial digestion and their uptake and impact on intestinal cells. *Toxicology in Vitro, 96*, Article 105772. https://doi.org/10.1016/j.tiv.2024.105772

Singh, N., Jenkins, G. J. S., Nelson, B. C., Marquis, B. J., Maffeis, T. G. G., Brown, A. P., … Doak, S. H. (2012). The role of iron redox state in the genotoxicity of ultrafine superparamagnetic iron oxide nanoparticles. *Biomaterials, 33*(1), 163–170. https://doi.org/10.1016/j.biomaterials.2011.09.087

Song, H., Zhang, X., Chen, T., & Jia, X. (2014). One-pot synthesis of bundle-like β-FeOOH nanorods and their transformation to porous α-Fe2O3 microspheres. *Ceramics International, 40*(10, Part A), 15595–15602. https://doi.org/10.1016/j.ceramint.2014.07.037

Torasso, N., Vergara-Rubio, A., Pereira, R., Martinez-Sabando, J., Baudrit, J. R. V., Cerveny, S., & Goyanes, S. (2023). An *in situ* approach to entrap ultra-small iron oxide nanoparticles inside hydrophilic electrospun nanofibers with high arsenic adsorption. *Chemical Engineering Journal, 454*, Article 140168. https://doi.org/10.1016/j.cej.2022.140168

Valsesia, A., Quarato, M., Ponti, J., Fumagalli, F., Gilliland, D., & Colpo, P. (2021). Combining microcavity size selection with Raman microscopy for the characterization of Nanoplastics in complex matrices. *Scientific Reports, 11*(1), 362. https://doi.org/10.1038/s41598-020-79714-z

Venator. (2019). Report on E171 (titanium dioxide) and E172 (iron oxide)—Analytical perspectives from research. , April https://www.efsa.europa.eu/sites/default/files/event/Presentation%205%20_%20David%20Brizzolara.pdf.

Verleysen, E., Wagner, T., Lipinski, H.-G., Kägi, R., Koeber, R., Boix-Sanfeliu, A., De Temmerman, P.-J., & Mast, J. (2019). Evaluation of a TEM based approach for size measurement of particulate (nano) materials. *Materials, 12*(14), 2274.

Voss, L., Hsiao, I.-L., Ebisch, M., Vidmar, J., Dreiack, N., Böhmert, L., … Sieg, H. (2020). The presence of iron oxide nanoparticles in the food pigment E172. *Food Chemistry, 327*, Article 127000. https://doi.org/10.1016/j.foodchem.2020.127000

Voss, L., Yilmaz, K., Burkard, L., Vidmar, J., Stock, V., Hoffmann, U., … Sieg, H. (2020). Impact of iron oxide nanoparticles on xenobiotic metabolism in HepaRG cells. *Archives of Toxicology, 94*(12), 4023–4035. https://doi.org/10.1007/s00204-020-02904-1

Winkler, A., Fumagalli, F., Cella, C., Gilliland, D., Tremolada, P., & Valsesia, A. (2022). Detection and formation mechanisms of secondary nanoplastic released from drinking water bottles. *Water Research, 222*, Article 118848. https://doi.org/10.1016/j.watres.2022.118848

Wouters, C., Kestens, V., Verleysen, E., & Mast, J. (2025). Assessing particle count in electron microscopy measurements of nanomaterials to support regulatory guidance. *Scientific Reports, 15*(1), 11803. https://doi.org/10.1038/s41598-025-92266-4

Wu, L., Wen, W., Wang, X., Huang, D., Cao, J., Qi, X., & Shen, S. (2022). Ultrasmall iron oxide nanoparticles cause significant toxicity by specifically inducing acute oxidative stress to multiple organs. *Particle and Fibre Toxicology, 19*(1), 24. https://doi.org/10.1186/s12989-022-00465-y

Yadav, P., Bhaduri, A., & Thakur, A. (2023). Manganese oxide nanoparticles: An insight into structure, synthesis and applications. *ChemBioEng Reviews, 10*(4), 510–528. https://doi.org/10.1002/cben.202200056

Yibin, X., Masayoshi, Y., & Pierre, V. (2011). Inorganic materials database for exploring the nature of material. *Japanese Journal of Applied Physics, 50*(11S), Article 11RH02.